Icarus 237 (2014) 211–238

Contents lists available at ScienceDirect

Icarus

journal homepage: www.elsevier.com/locate/icarus

Neptune's global circulation deduced from multi-wavelength observations

Imke de Pater [a,b,c,*], Leigh N. Fletcher [d], Statia Luszcz-Cook [j], David DeBoer [a], Bryan Butler [e], Heidi B. Hammel [f,g], Michael L. Sitko [i], Glenn Orton [h], Philip S. Marcus [k]

[a] Astronomy Department, University of California, 601 Campbell Hall, Berkeley, CA 94720, USA
[b] Faculty of Aerospace Engineering, Delft University of Technology, NL-2629 HS Delft, The Netherlands
[c] SRON Netherlands Institute for Space Research, 3584 CA Utrecht, The Netherlands
[d] Atmospheric, Oceanic & Planetary Physics, Department of Physics, University of Oxford, Clarendon Laboratory, Parks Road, Oxford OX1 3PU, UK
[e] National Radio Astronomy Observatory, Socorro, NM 87801, USA
[f] Association of Universities for Research in Astronomy, 1212 New York Avenue NW, Suite 450, Washington, DC 20005, USA
[g] Space Science Institute, 4750 Walnut Street, Suite 205, Boulder, CO 80301, USA
[h] Jet Propulsion Laboratory, MS 169-237, California Institute of Technology, 4800 Oak Grove Drive, Pasadena, CA 91109, USA
[i] Department of Physics, University of Cincinnati, Cincinnati, OH 45221-0011, USA
[j] Department of Astrophysics, American Museum of Natural History, 79th Street at Central Park West, New York, NY 10024, USA
[k] Department of Mechanical Engineering, University of California, 6121 Etcheverry Hall, Berkeley, CA 94720, USA

ARTICLE INFO

Article history:
Received 23 October 2013
Revised 15 February 2014
Accepted 26 February 2014
Available online 13 March 2014

Keywords:
Neptune, atmosphere
Infrared observations
Radio observations

ABSTRACT

We observed Neptune between June and October 2003 at near- and mid-infrared wavelengths with the 10-m W.M. Keck II and I telescopes, respectively; and at radio wavelengths with the Very Large Array. Images were obtained at near-infrared wavelengths with NIRC2 coupled to the adaptive optics system in both broad- and narrow-band filters between 1.2 and 2.2 μm. In the mid-infrared we imaged Neptune at wavelengths between 8 and 22 μm, and obtained slit-resolved spectra at 8—13 μm and 18—22 μm. At radio wavelengths we mapped the planet in discrete filters between 0.7 and 6 cm.

We analyzed each dataset separately with a radiative-transfer program that is optimized for that particular wavelength regime. At southern midlatitudes the atmosphere appears to be cooler at mid-infrared wavelengths than anywhere else on the planet. We interpret this to be caused by adiabatic cooling due to air rising at midlatitudes at all longitudes from the upper troposphere up to $\lesssim$0.1 mbar levels. At near-infrared wavelengths we find two distinct cloud layers at these latitudes: a relatively deep layer of clouds (presumably methane) in the troposphere at pressure levels $P \sim$ 300–$\gtrsim$600 mbar, which we suggest to be caused by the large-scale upwelling and its accompanying adiabatic cooling and condensation of methane; and a higher, spatially intermittent, layer of clouds in the stratosphere at 20–30 mbar. The latitudes of these high clouds encompass an anticyclonic band of zonal flow, which suggests that they may be due to strong, but localized, vertical upwellings associated with local anticyclones, rather than plumes in convective (i.e., cyclonic) storms. Clouds at northern midlatitudes are located at the highest altitudes in the atmosphere, near 10 mbar.

Neptune's south pole is considerably enhanced in brightness at both mid-infrared and radio wavelengths, i.e., from ~0.1 mbar levels in the stratosphere down to tens of bars in the troposphere. We interpret this to be due to subsiding motions from the stratosphere all the way down to the deep troposphere. The enhanced brightness observed at mid-infrared wavelengths is interpreted to be due to adiabatic heating by compression in the stratosphere, and the enhanced brightness temperature at radio wavelengths reveals that the subsiding air over the pole is very dry; the relative humidity of H_2S over the pole is only 5% at altitudes above the NH_4SH cloud at ~40 bar. The low humidity region extends from the south pole down to latitudes of 66°S. This is near the same latitudes as the south polar prograde jet signifying the boundary of the polar vortex. We suggest that the South Polar Features (SPFs) at latitudes of 60–70° are convective storms, produced by baroclinic instabilities expected to be produced at latitudes near the south polar prograde jet.

* Corresponding author at: Astronomy Department, University of California, 601 Campbell Hall, Berkeley, CA 94720, USA. Fax: +1 510 642 3411.
E-mail address: imke@berkeley.edu (I. de Pater).

http://dx.doi.org/10.1016/j.icarus.2014.02.030

Taken together, our data suggest a global circulation pattern where air is rising above southern and northern midlatitudes, from the troposphere up well into the stratosphere, and subsidence of dry air over the pole and equator from the stratosphere down into the troposphere. We suggest that this pattern extends all the way from $\lesssim$0.1 mbar down to pressures of $\gtrsim$40 bar.

1. Introduction

After its discovery in 1846 by J.G. Galle, physical studies of the planet Neptune were limited due to the planet's extreme distance and thus small angular size (diameter of order 2.3″). It was evident early on from ground-based photometry and images that Neptune was an extremely dynamic planet (Hammel, 1989 and references therein). Our understanding got a tremendous boost with the Voyager flyby in 1989, when the first highly detailed images were returned to Earth (Smith et al., 1989). These images revealed a Great Dark Spot (GDS) on Neptune at a latitude of ~20°S, a smaller dark spot (DS2) at ~55°S, a bright compact feature near 42°S (Scooter), and a bright feature at ~71°S, dubbed a South Polar Feature (SPF). A bright cloud feature seen in groundbased near-infrared (NIR) data was identified as a collection of companion clouds to the GDS. With the launch of the Hubble Space Telescope (HST), scientists were able to continue observing Neptune at a relatively high angular resolution (e.g., Sromovsky et al., 1995, 2001a,b, 2003; Hammel et al., 1995; Hammel and Lockwood, 1997). A highlight of these observations was the disappearance of the GDS. With the advent of adaptive optics (AO), Neptune could be observed from the ground at NIR wavelengths at angular resolutions that rival the Hubble data (e.g., Roddier et al., 1998; Max et al., 2003; Gibbard et al., 2002, 2003; de Pater et al., 2005a; Luszcz-Cook et al., 2010; Irwin et al., 2011; Martin et al., 2012). In these images Neptune is characterized as a planet with very bright circumferential bands at both southern and northern midlatitudes, as well as occasionally an extremely bright SPF. The latitudinal bands of clouds consist of individual small elongated cloud features.

While Neptune is detected in reflected sunlight at visible and NIR wavelengths, the thermal emission from its troposphere and stratosphere can be studied in both the mid-infrared (MIR) and the radio spectrum. Voyager observations in the MIR revealed the planet's large internal heat source: Neptune emits a thermal flux about 2.6 times larger than the mean solar flux absorbed by its atmosphere (Pearl and Conrath, 1991). Such a high heat flow would naturally predict a highly dynamic atmosphere, as observed. Voyager IRIS data at 200–450 cm^{-1} (22—50 μm) and at 729 cm^{-1} (13.7 μm) further revealed latitudinal variations in brightness, with maxima near the equator and at the south pole, and a minimum at southern midlatitudes. Conrath et al. (1991) and Bézard et al. (1991) inferred from this pattern a meridional circulation of upwelling at southern midlatitudes and subsidence at low (near the equator) and high latitudes.

The first radio astronomical detection was made in 1966 by Kellermann and Pauliny-Toth (1966) at 1.9 cm; in subsequent decades the planet's disk-averaged radio spectrum at mm–cm wavelengths was measured. Even though the early observations had relatively large uncertainties, it became clear that Neptune, like Uranus, was much warmer than expected for a solar-composition atmosphere. Since the microwave absorption by ammonia gas dominates the opacity in a solar-composition atmosphere, the observations could only be explained if, somehow, the atmosphere were substantially depleted in NH_3 gas. This could be brought about if the H_2S abundance on Neptune were larger than that of NH_3, in which case the formation of NH_4SH would effectively eliminate ammonia gas from Neptune's troposphere, enabling one to probe deeper warmer layers in the planet's atmosphere (e.g., Gulkis et al., 1978; Lewis and Prinn, 1980; de Pater and Richmond, 1989). Good fits to the data are obtained if H_2S gas is enhanced by a factor of ~30–60 above the protosolar S/H abundance,[1] while NH_3 in Neptune's deep atmosphere should not exceed the solar N value (de Pater et al., 1991; deBoer and Steffes, 1996). Higher abundances of H_2S push the NH_4SH cloud deeper into the atmosphere, and increase the line-of-sight microwave opacity due to H_2S.

In order to further investigate Neptune's global circulation and potential changes therein, we observed the planet in 2003 at NIR and MIR wavelengths with the 10-m W.M. Keck telescopes in Hawaii, and at radio wavelengths with the Very Large Array (VLA) in New Mexico. Our goal was to observe the planet at high spatial resolution in all three wavelength regimes at roughly the same time to deduce Neptune's global circulation pattern from the deep troposphere upwards, well into the stratosphere. For practical reasons, the data were taken over a time period of a few months, i.e., short compared to Neptune's orbital period (164 years). Although individual cloud features observed at NIR wavelengths do change over this period, the general circulation will not.

Preliminary reports of our datasets have been presented by Martin et al. (2008); no quantitative analysis was presented, however. Some of the NIR observations were published by de Pater et al. (2005a) in a paper focused on Neptune's rings; the planet's atmosphere was not discussed at that time. In this paper we present the full data sets along with analyses; the analysis of the MIR dataset, however, was presented by Fletcher et al. (2014), and we only present a summary of their findings in this paper. In Section 2 we present all three data sets (NIR, MIR and radio). Separate analyses of each data set are presented in Sections 3–5. An overall synthesis, tying the data sets together is provided in Section 6, with a summary of our conclusions in Section 7.

2. Observations and data reduction

Over a 4-month period in 2003, from June to October, we observed Neptune at NIR, MIR and radio wavelengths. The observations are summarized in Table 1, ordered in wavelength from short to long.

2.1. Near-infrared observations

NIR observations were taken UT October 3–6, 2003 using the Near Infrared Camera 2 (NIRC2) coupled to the adaptive optics (AO) system at the W.M. Keck II telescope in Mauna Kea, Hawaii (Wizinowich et al., 2000). NIRC2 has a 1024 × 1024 Aladdin-3 InSb array detector, which we used in its high angular resolution mode, i.e., the NARROW camera at 9.94 ± 0.03 mas per pixel (de Pater et al., 2006), which corresponds to 213 km at Neptune's distance during our observations. On all 4 days, we observed Neptune in the J, H and K′ bands; on October 4, 5 and 6 we observed the planet also with several narrow-band filters, as summarized in Table 2. de Pater et al. (2005a) report a Strehl ratio SR = 0.5 at K′ band, and SR = 0.3—0.4 at H. Strehl ratios in the narrow-band

[1] We use the protosolar elemental ratios for C, N, O, and S from Asplund et al. (2009): C/H_2 = 5.90E−4; N/H_2 = 1.48E−4; O/H_2 = 1.07E−3; S/H_2 = 2.89E−5.

Table 1
Summary of Neptune observations in 2003.

Telescope/instr.	Wavelength (range)	Date (UT)	r[a] (AU)	Δ[a] (AU)	Diam. (″)	D_E[b] (°)	Pixel size (″)	Pixel size[c] (km)
Keck/NIRC2	Near-IR	2003–10–03	30.077	29.552	2.31	−28.98	0.00994	213
Keck/NIRC2	Near-IR	2003–10–04	30.077	29.567	2.31	−28.98	0.00994	213
Keck/NIRC2	Near-IR	2003–10–05	30.077	29.582	2.31	−28.98	0.00994	213
Keck/NIRC2	Near-IR	2003–10–06	30.077	29.597	2.31	−28.98	0.00994	213
Keck/LWS	Mid-IR	2003–09–05	30.078	29.213	2.34	−29.02	0.0847	1794
Keck/LWS	Mid-IR	2003–09–06	30.078	29.222	2.34	−29.02	0.0847	1795
VLA/Q-Band	0.7 cm	2003–10–12	30.077	29.688	2.30	−28.98	0.02	431
VLA/K-Band	1.3 cm	2003–10–11	30.077	29.704	2.30	−28.98	0.03	646
VLA/Ku-Band	2 cm	2003–06–26	30.080	29.276	2.33	−29.16	0.03	637
VLA/X-Band	3.6 cm	2003–06–27	30.080	29.266	2.33	−29.16	0.05	1061
VLA/C-Band	6 cm	2003–06–28	30.080	29.256	2.33	−29.15	0.1	2122

[a] r and Δ are the heliocentric and geocentric distance of Neptune, respectively.
[b] Sub-Earth latitude.
[c] Pixel size refers to the size of a pixel in km at the center of the disk.

filters are also typically between 0.3 and 0.6. The angular resolution, as given by the full width at half maximum (FWHM) of unresolved features on Neptune's disk, is typically between 0.038″ and 0.05″ (Table 2), i.e., close to the diffraction limit of the telescope.

We reduced images using standard infrared data reduction techniques of sky subtraction, flat-fielding and median-value masking to remove hot and cold pixels. The broad-band images were not averaged, but kept as single 1-min frames. The signal-to-noise (SNR) in such frames is high, and averaging would lead to a slight smearing of the cloud features. Sets of narrowband images (2–5 in number, Table 2) were averaged together to increase the SNR. The data were photometrically calibrated using the infrared standard star HD 201941 (Elias et al., 1982). Although the photometric accuracy based on our stellar images (4 in each filter, on each day) was better then 5%, we adopt a more conservative uncertainty of order 10–15% to account for possible photometric fluctuations throughout the night.

We converted the observed flux densities, F_N, to the dimensionless parameter I/F, where I is the reflected intensity and πF the solar flux density at Neptune's distance (e.g., Hammel, 1989):

$$\frac{I}{F} = \frac{r^2}{\Omega}\frac{F_N}{F_\odot}, \tag{1}$$

with r Neptune's heliocentric distance, $\pi F_\odot$ the Sun's flux density at Earth's orbit (taken from Colina et al., 1996), and Ω is the solid angle (in steradians) subtended by the body or a pixel on the detector. By this definition, $I/F = 1$ for diffuse scattering from a Lambertian surface, and is equal to the geometric albedo if the object is observed at normal incidence and a solar phase angle of 0°.

Table 2
Summary of NIR images in 2003.

Wavelength (μm)	Bandpass (μm)	UT Date (yr–mm–dd)	Time range (hr:mm–hr:mm)	Image #	Airmass	Int. time (s/frame)	FWHM[a] (″)	FWHM[b] (km)
1.25 (J-band)	1.17–1.33	2003–10–03	06:55–07:01	137–141	1.27	60	0.045	645
1.63 (H-band)	1.48–1.78	2003–10–03	06:30–06:37	122–126	1.26	60	0.046	659
2.12 (K′-band)	1.95–2.30	2003–10–03	07:04–07:13	142–146	1.28	60	0.045	645
1.25 (J-band)	1.17–1.33	2003–10–04	06:01–06:04	172–174	1.27	60	0.038	545
1.63 (H-band)	1.48–1.78	2003–10–04	05:45–05:53	163–168	1.27	60	0.045	645
1.63 (H-band)	1.48–1.78	2003–10–04	08:03–08:11	230–235	1.42	60	0.045	645
2.12 (K′-band)	1.95–2.30	2003–10–04	06:07–06:29	175–189	1.26	60	0.048	688
2.12 (K′-band)	1.95–2.30	2003–10–04	08:13–08:21	236–241	1.46	60	0.048	688
1.29 (Pabeta)	1.28–1.30	2003–10–04	06:43–06:51	195–199	1.27	60	0.045	645
1.58 (Hcont)	1.57–1.59	2003–10–04	06:42–06:41	190–194	1.26	60	0.050	717
1.65 (FeII)	1.63–1.66	2003–10–04	06:52–07:01	200–204	1.27	60	0.050	717
2.06 (HeIB)	2.04–2.07	2003–10–04	07:47–07:55	223–227	1.38	60	0.047	674
1.25 (J-band)	1.17–1.33	2003–10–05	05:42–05:46	174–176	1.28	60	0.046	660
1.25 (J-band)	1.17–1.33	2003–10–05	07:49–07:53	235–237	1.38	60	0.046	660
1.63 (H-band)	1.48–1.78	2003–10–05	06:06–06:14	186–190	1.26	60	0.049	703
1.63 (H-band)	1.48–1.78	2003–10–05	08:04–08:08	244–246	1.42	60	0.049	703
2.12 (K′-band)	1.95–2.30	2003–10–05	05:57–06:04	183–185	1.26	60	0.045	645
2.12 (K′-band)	1.95–2.30	2003–10–05	08:30–08:33	257–258	1.53	60	0.045	645
1.29 (Pabeta)	1.28–1.30	2003–10–05	08:10–08:18	247–251	1.46	60	0.043	617
1.65 (FeII)	1.63–1.66	2003–10–05	08:18–08:33	252–256	1.50	60	0.038	545
1.25 (J-band)	1.17–1.33	2003–10–06	06:39–06:42	250–252	1.26	60	0.044	631
1.25 (J-band)	1.17–1.33	2003–10–06	08:04–08:06	292–293	1.43	60	0.044	631
1.63 (H-band)	1.48–1.78	2003–10–06	06:23–06:28	241–243	1.26	60	0.046	660
1.63 (H-band)	1.48–1.78	2003–10–06	07:59–08:02	290–291	1.42	60	0.046	660
2.12 (K′-band)	1.95–2.30	2003–10–06	06:00–06:22	226–240	1.26	60	0.045	646
2.12 (K′-band)	1.95–2.30	2003–10–06	07:45–07:53	281–285	1.38	60	0.045	646
1.58 (Hcont)	1.57–1.59	2003–10–06	08:16–08:19	298–299	1.48	60	0.048	689
1.65 (FeII)	1.63–1.66	2003–10–06	08:12–08:15	296–297	1.47	60	0.048	689
2.06 (HeIB)	2.04–2.07	2003–10–06	08:08–08:11	294–295	1.45	60	0.050	718
2.17 (Brgamma)	2.15–2.18	2003–10–06	08:16–08:19	300–301	1.48	60	∼0.05	720
2.27 (Kcont)	2.26–2.29	2003–10–06	08:12–08:15	302–303	1.47	60	∼0.05	720

[a] FWHM (Full Width at Half Maximum) as determined from unresolved features on Neptune's disk (in many cases the south polar dot).
[b] FWHM in km at the center of Neptune's disk.

Fig. 1 shows images in H and K′ bands on all 4 days. The images in H and K′ band were usually taken one after the other to minimize rotation of the planet between images. The planet rotates by 1.5 rotation periods between successive days, so that roughly the same longitudinal aspect is seen on images separated by 2 days (3 rotations). Bright bands of discrete cloud features are always visible between ~30°S and 50°S and between ~25°N and 40°N, as well as several discrete cloud features near 60–70°S; these are the SPFs (Smith et al., 1989). SPFs are highly variable in brightness and appear and disappear at random times (e.g., Rages et al., 2002; Fitzpatrick et al., 2013), as confirmed by the series of images in Fig. 1. A small feature at the south pole is clearly visible in H band and not, or barely, at K′. Luszcz-Cook et al. (2010) showed that this south polar "dot" may not always be one cloud centered exactly at the south pole; they reported a double spot on one day in 2007, and a single one 2 days later, both offset by a few degrees from the south pole. Faint clouds can be discerned in the equatorial region. Such features have been reported before by, e.g., Max et al. (2003), Irwin et al. (2011), and Martin et al. (2012). Fig. 1 shows that, although the global pattern of cloud activity does not change much over this time period, a detailed comparison shows the clouds to brighten and dim, appear and disappear at least as quickly as 3 rotations of the planet.

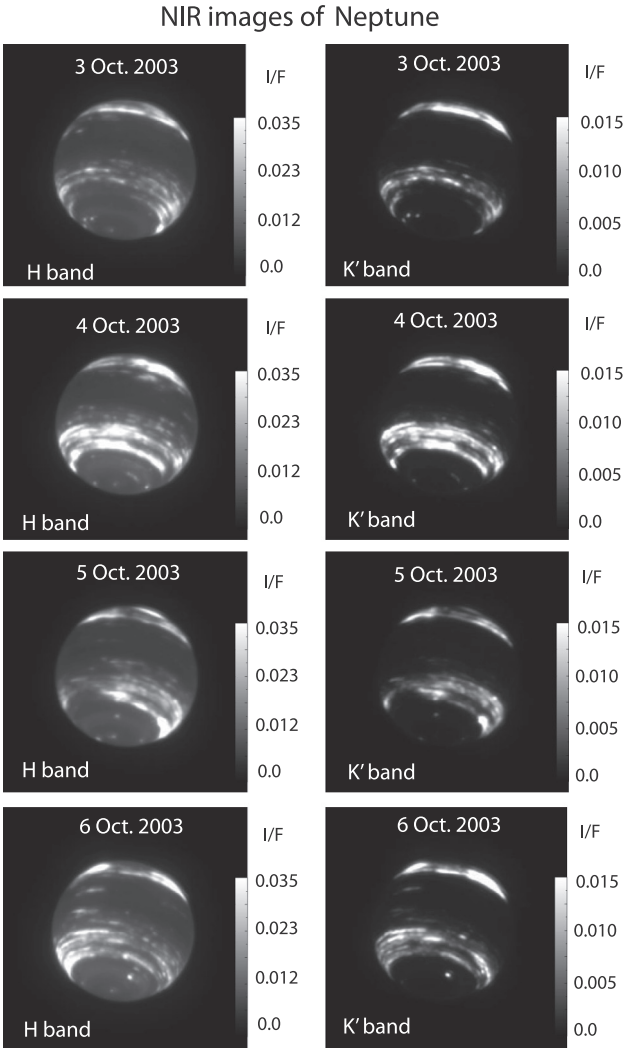

Fig. 1. NIR images of Neptune taken with NIRC2 on the Keck II telescope in H band (1.6 μm; left) and K′ band (2.2 μm; right). We show both sets of images since they probe different depths in the atmosphere. In K′ band we only see clouds in the upper troposphere and stratosphere, while in H band we probe deeper layers. For example, a feature at the south pole is only seen in H band and not in K′, which indicates that this feature must be located at pressures $\gtrsim 1$ bar. As shown, the images reveal the spatial distribution of clouds and hazes on the two days, which change from day-to-day and between wavelengths. The I/F scale is shown on the right side for each image. The position angle of Neptune's north pole is ~349° measured from North towards astronomical East.

2.2. Mid-infrared observations

2.2.1. Images

On UT September 5 and 6, 2003, we imaged Neptune through broad-band filters using the Long Wavelength Spectrometer (LWS) at the W.M. Keck I telescope in Mauna Kea, Hawaii. The LWS detector is a 128 × 128 Boeing Si:As array, with a pixel size of 0.0847″ (Jones and Puetter, 1993), which corresponds to 1788 km at Neptune's geocentric distance on the dates of these observations. We used a total of 8 filters between 8 and 22 μm, as summarized in Table 3. We used the standard chop-nod mode for the data acquisition, at an amplitude of 10″ and an integration time of 0.01 s per frame; the total integration time per image, i.e., after properly co-adding the frames, is indicated in the table. Chopping is performed to cancel out sky radiation, and nodding, in a direction opposite to that of chopping, is used to cancel out the telescope contribution to the background emission. The combined chop-nod mode is very efficient to cancel out all background radiation. After properly combining the images in the chop-nod data-cubes, the resulting image was divided by a flat field which was created from the sky images which were extracted from the chop-nod data-cubes, and bad pixels were replaced with the median of the neighboring pixels. The data were calibrated using the infrared standard star HD199345 (Cohen et al., 1999). In order to convert the number of counts received by our detector in each filter, we convolved the filter function with the telluric transmission, where the latter was provided by H.G. Roe using his custom code BFATS (Brute Force Atmospheric Transmission Simulator) for a "standard" terrestrial atmosphere with 1.6 mm of precipitable water and an airmass of 1.5 (Roe, 2002) (Table 3). Our derived flux density numbers (Table 4) agree well with those listed on the Keck website,[2] except at 8.0 μm, where our derived flux density is ~10% smaller. Based upon the quality of the images during the night, we adopt a (conservative) calibration uncertainty of 10% at all wavelengths; this uncertainty also encompasses potential differences in the actual column of water vapor above Mauna Kea at the time. The pixel values were also converted to brightness temperature.

To increase the SNR, we coadded all images of Neptune in a given filter. The results are shown in Fig. 2; the point spread function (PSF) at each wavelength is shown as an inset on each image. The angular resolution is close to the diffraction limit of the telescope, which is 0.20″ at a wavelength of 8 μm, and increases with wavelength up to 0.55″ at 22 μm. In the methane band (8.0 and 8.9 μm), the disk is slightly limb-brightened with a bright south polar region. In the ethane band (11.7 and 12.5 μm), limb-brightening and the south polar region are very pronounced. Limb-brightening is a clear sign of probing the stratosphere: higher altitudes are probed near the limb, and since the temperature is rising with altitude in the stratosphere, the planet will be limb-brightened. As shown from the PSF, slight east–west asymmetries most likely result from asymmetries in the PSF. At 17.65, 18.75 and 22 μm the equatorial region is slightly enhanced in intensity (25–50% in radiance, or ~2 K in brightness) compared to the southern midlatitudes and the south polar region is very bright. These same features are also visible at 10.7 μm. These characteristics are consistent with later imaging at similar wavelengths by Hammel et al.

[2] http://www2.keck.hawaii.edu/inst/lws/lws_stds_ra.list.

Table 3
Summary of MIR observations in 2003.

Name	Bandpass[a] (μm)	UT Date (yr-mm-dd)	Time range (hr:mm–hr:mm)	Image #	Airmass	Int. time (sec per frame)	FWHM[b] (″)	FWHM[c] (km)	Comments[d]
Images									
N band									
8.0	7.81–8.94	2003–09–05	06:18–06:27	49–50	1.48	190	0.36	7630	H_2, CH_4
8.0	7.81–8.94	2003–09–05	07:46–07:58	62–63	1.27	286	0.36	7630	H_2, CH_4
8.9	8.39–9.27	2003–09–05	06:09–06:17	47–48	1.52	190	0.26	5510	H_2, CH_4
8.9	8.39–9.27	2003–09–05	08:00–08:13	64–65	1.27	286	0.26	5510	H_2, CH_4
10.7	9.92–11.47	2003–09–05	06:28–06:41	51–52	1.43	238	0.35	7415	H_2, C_2H_4
10.7	9.92–11.47	2003–09–05	08:14–08:27	66–67	1.26	286	0.35	7415	H_2, C_2H_4
11.7	11.15–12.25	2003–09–05	05:59–05:58	43–44	1.64	190	0.34	7200	H_2, C_2H_6
11.7	11.15–12.25	2003–09–05	07:33–07:45	60–61	1.29	286	0.34	7200	H_2, C_2H_6
12.5	12.01–13.25	2003–09–05	05:49–06:08	45–46	1.56	190	0.33	6990	H_2, C_2H_6, C_2H_2
12.5	12.01–13.25	2003–09–05	07:25–07:30	59	1.30	143	0.33	6990	H_2, C_2H_6, C_2H_2
Q band									
17.65	17.31–18.16	2003–09–05	07:11–07:24	57–58	1.32	286	0.53	11,230	H_2
17.65	17.31–18.16	2003–09–05	08:48–08:42	68–69	1.26	286	0.53	11,230	H_2
18.75	18.31–19.20	2003–09–05	06:42–07:10	53–56	1.40	572	0.55	11,650	H_2
22.0	20.87–22.96	2003–09–06	09:55–10:10	60–61	1.40	286	0.52	11,020	H_2
Spectra									
Nwide	8.1–12.9	2003–09–06	06:15–06:50	37–40	1.43	576	0.508	10,766	North–South
Nwide	8.1–12.9	2003–09–06	07:05–07:43	42–45	1.31	576	0.508	10,766	East–West
Spec20	17.6–22.4	2003–09–06	08:39–09:28	53–56	1.30	768	0.508	10,766	North–South

[a] Images: Bandpass between half power points. Spectra: Spectral coverage of band.
[b] FWHM (full width at half maximum) for images, as determined from stars. Slit width (6 pixels) for spectra.
[c] FWHM in km at disk center.
[d] Primary gas opacities for images; Slit orientation on Neptune for spectra.

Table 4
Summary of MIR flux densities for HD199345.

Name	Bandpass[a] (μm)	Flux density[b] ($W/cm^2/\mu m$)
8.0	7.81–8.94	3.51215e−17
8.9	8.39–9.27	3.00316e−17
10.7	9.92–11.47	1.54657e−17
11.7	11.15–12.25	1.10870e−17
12.5	12.01–13.25	8.20157e−18
17.65	17.31–18.16	2.05959e−18
18.75	18.31–19.20	1.67550e−18
22.0	20.87–22.96	1.01282e−18

[a] Bandpass between half power points.
[b] Flux densities as derived by us from the filter functions.

(2007) and Orton et al. (2007a). Although Orton et al. found that the bright spot near the south pole was offset from the south pole, our images and those published in Hammel et al. (2007) do not show evidence for an offset (see Orton et al. (2012) for more details on potential offsets).

2.2.2. Spectra

On September 6, 2003, we obtained low-resolution N (8.1—12.9 μm) and Q (17.6—22.4 μm) band spectra. We used a 6-pixel wide slit; with a pixel size of 0.0847″/pixel this translates to a slit width of 0.5″. The total slit length is 10.24″. A total of 128 pixels covers the wavelength range, providing a pixel spacing of $\Delta\lambda = 0.03737$ μm in the N band, and $\Delta\lambda = 0.0370$ μm in the Q band. The standard stars HD198542 and HD188154 (Cohen et al., 1999) were used for both telluric (and filter-response) corrections and photometric calibration. We first fine-tuned the wavelength scale by matching the stellar spectra to the Earth's atmospheric transmission curve (Fig. 3). This is relatively straightforward in N band by simply lining up the spectra to match the strong terrestrial O_3 band near 9.5 μm. This resulted in shifts of ~0.3 μm in N band relative to the initially adopted wavelength scale, while the wavelength spacing was not affected. In Q band the stellar spectra more or less matched the overall slope in the transmission curve, and the drop near 17.6 μm, so we did not change the Q band wavelength scale. Based on a comparison of different stellar spectra we adopt an uncertainty of 0.04 μm in our wavelength scale. Using the appropriately shifted stellar spectra, we determined the telluric and photometric calibration independently from both stars; these agreed with one another to within ~3%. The Neptune spectra were calibrated by using the average of the two stellar correction curves.

Since only a fraction of a star's flux density is measured in the slit, we need to correct for slit-losses before we can photometrically calibrate Neptune. We determined the stellar slit-loss by overlaying a slit (i.e., a rectangle with the proper slit dimensions) on images obtained of the same star just prior to the spectroscopy; these images had also been used to position the slit accurately on the star. We calculated the fraction of the flux density received in the slit on each of the images, which resulted in a median value of $66 \pm 6\%$. We adopt a total photometric uncertainty in the Neptune spectra of order 10–15%. This number is based both on the uncertainty in slit-loss, and on a much more conservative estimate for absolute photometry (~10%) than the ~3% inferred from our stellar spectra.

In the N band we oriented the slit once along Neptune's central meridian, and once orthogonal to its central meridian; in the Q band we obtained a single spectrum along Neptune's central meridian. We derive disk-integrated spectra from our data to allow for direct comparison with the spectra published by Hammel et al. (2006), using a technique analogous to that used to determine the stellar slit-loss. That is, we overlaid the rectangular slit on the images we had obtained in the eight different filters. We then calculated the fraction of the emission observed by integrating the emission on the image within this rectangular strip, as well as the total emission received in that filter. In the N band we determined this for both slit positions, and averaged the results for each filter. The resulting emission was $21.5 \pm 1\%$ of the total disk-integrated intensity, and hence we multiplied the N band spectrum

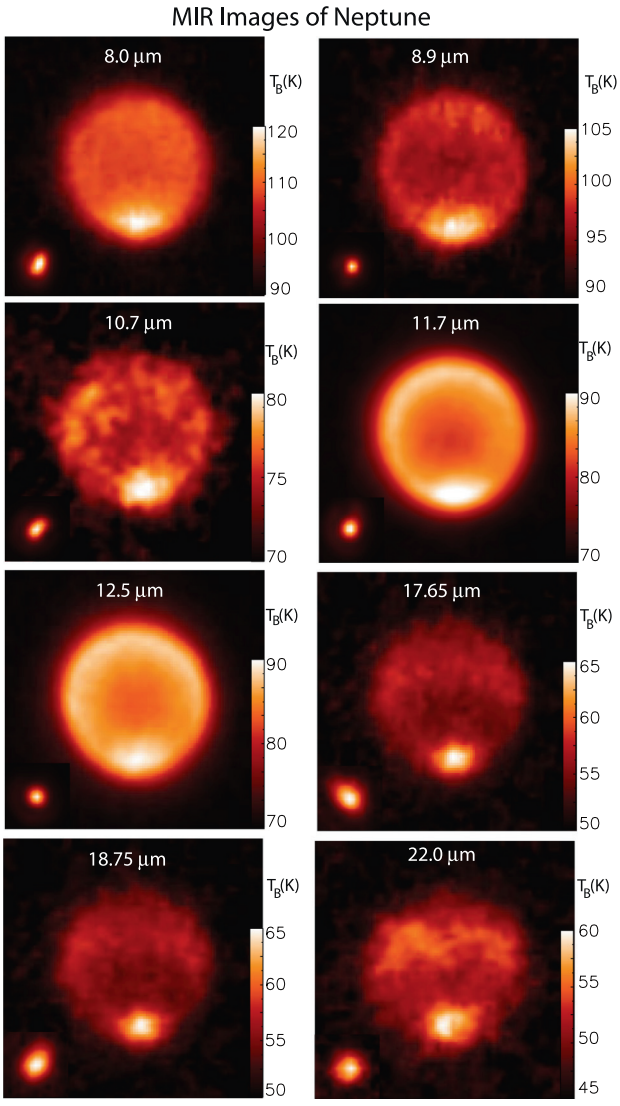

Fig. 2. MIR images of Neptune taken with LWS on the Keck I telescope in the 8.0 μm, 8.9 μm, 10.7 μm, 11.7 μm, 12.5 μm, 17.65 μm, 18.75 μm and 22 μm filters. The PSF at each wavelength is shown in the lower left corner of the image, on a linear scale from 0 to the maximum value of 1; the approximate brightness temperature scale in K is shown on the right. Neptune has been rotated in these images so that its north pole is pointing up.

by 4.65 to obtain a disk-integrated N band spectrum. In the Q band we received $24 \pm 1\%$ of the total intensity, and hence multiplied the observed Q band spectrum by a factor of 4.05 to obtain the total disk-integrated Q band spectrum. The uncertainty in these spectra is dominated by the photometric uncertainty described above, i.e., 10–15%. Assuming all emission to arise from the disk of Neptune, we converted the observed flux units to W cm^{-2} - μm^{-1} sr^{-1}. The resulting spectra are shown in Fig. 4, with Hammel et al.'s (2006) spectrum superposed. The latter spectrum was obtained with the Broadband Array Spectrograph System (BASS; Hackwell et al., 1990) on NASA's Infrared Telescope Facility (IRTF); we recalibrated this spectrum, and hence it differs somewhat from that in the original publication. Before recalibration, the planet appeared to be anomalously bright near 12 μm compared to spectra taken before and after 2003; after recalibration this peak is lower. As shown, the Keck and BASS spectra agree reasonably well within the errorbars. Hence, the planet may not be as anomalously bright near 12 μm compared to spectra taken in other years as suggested by Hammel et al.; also, our data suggest that the planet may be brighter in the 8-μm window than indicated by the BASS spectrum. Similarly high 8-μm radiances were measured with the midIR camera Michelle on Gemini in 2005, and with ISAS/JAXA's AKARI infrared astronomy satellite in 2007 (Fletcher et al., 2014). As a consistency check, we superpose the total flux density from the individual images on the spectra.

Since we obtained spatially-resolved spectra along a slit, we can evaluate spectra at individual locations along the disk. In the Q band, given the SNR in individual spectra, no variations between spectra at different locations were discerned. In the N band the SNR is high, and clear variations in spectral shape are seen along the slit. As an example, in Fig. 5 we show spectra at three locations on Neptune's disk, chosen to be at the two maxima (north limb and south pole) and the minimum (center of disk) intensities along the slit. These variations are discussed further in Section 4.

2.3. Radio observations

Radio observations were conducted with the Very Large Array (VLA) on UT 26–28 June, 2003 at wavelengths of 2 cm (Ku band), 3.6 cm (X band), and 6 cm (C band) while the VLA was in its most extended "A" configuration. In the A configuration the nine antennas along each arm are spread over 21 km, giving a maximum baseline of 36 km. The shortest spacing in this array is about 680 meters. On UT 11 and 12 October, 2003, observations at 0.7 cm (Q band) and 1.3 cm (K band) were acquired in the "BnA" configuration. The BnA configuration is a hybrid array, where antennas along the east and west arm have moved to the B configuration, with a maximum baseline of 11.4 km, and minimum of 210 m; the north arm is still in the A configuration. This configuration, therefore, is ideal for sources at low declinations, since with the foreshortening of the north arm there still is angular resolution in the north–south direction comparable to that in the east–west direction. We observed for a total of 8 h at each wavelength, i.e., one track was 8 h. In addition to Neptune, this also includes time on the calibrators. The observations are summarized in Table 5.

The gain of the antennas was calibrated on 3C286, with a flux density tied to Cygnus A via the VLA internal calibration scale. Phase calibration was performed on the radio source 2131-121. Internal and absolute uncertainties in the flux densities are believed to be better than ~3% at 2–6 cm, and better than ~5% at 0.7 and 1.3 cm. Both the initial processing of the data, as flagging/editing and calibration, as well as the subsequent data reduction (see below) were done with the NRAO AIPS (Astronomical Image Processing Software) software (http://www.aips.nrao.edu/CookHTML/CookBook.html).

After normal calibration, a sequence of imaging and self-calibration cycles was performed. Self-calibration uses a model of the visibilities to derive antenna-based corrections to the visibilities so that the visibilities over time are self-consistent in the end (Butler et al., 2001). Each self-calibration and imaging step is based on a model of the visibilities that is based on the last image that was created from the self-calibrated data. Although in principle both the amplitude and phase can be corrected this way, we only corrected the phase of the visibilities. This sequence of self-calibration and imaging proceeded until the image quality (the rms in the image outside Neptune) started to degrade. A final image was made with natural weighting. The CLEAN components, i.e., the δ-components that represent Neptune after CLEANing (a deconvolution algorithm; Clark, 1980) the map, were added to the residual map after each component was convolved with a circular restoring beam, with a diameter equal to the major axis of the best-fit gaussian beam. The final images are shown in Fig. 6. The south polar region is bright in all images, although in this representation it is difficult to discern at 0.7 cm, due to the relatively poor SNR, and at 6 cm, because the large beam at this wavelength blurs

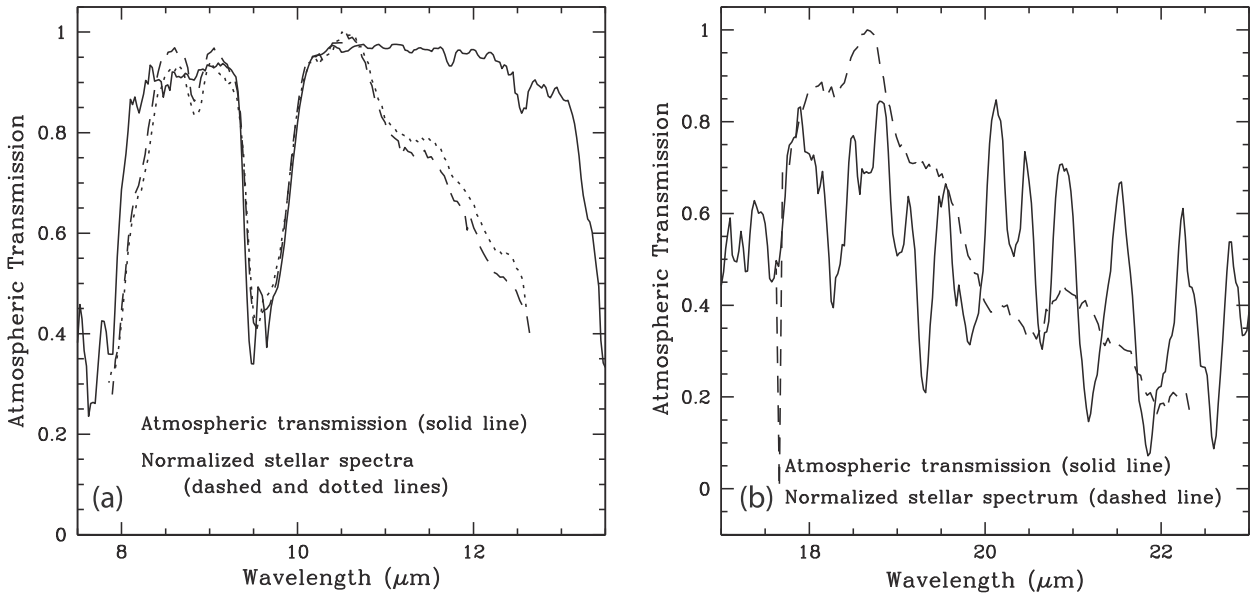

Fig. 3. Normalized (to unity) stellar spectra are superposed on atmospheric transmission curves for the N band (panel a) and the Q band (panel b) spectra. These plots were used to fine-tune the LWS wavelength scale of the spectra.

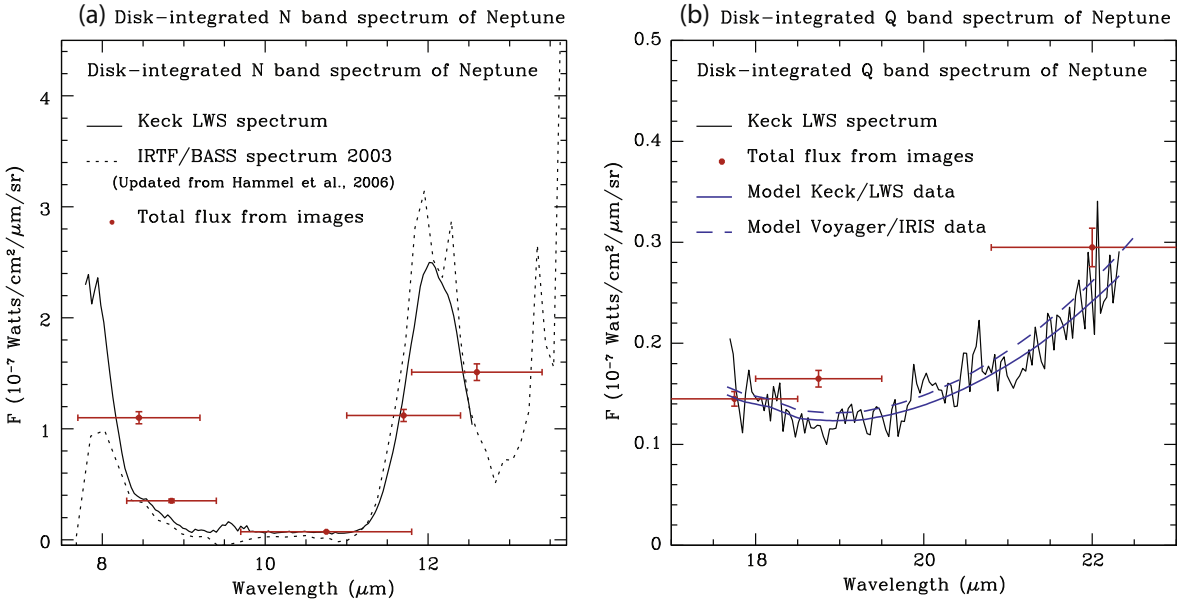

Fig. 4. (a) Disk-averaged N band spectrum of Neptune (solid line), with the IRTF BASS spectrum superposed (dotted line; adapted from Hammel et al., 2006). The BASS spectrum was taken ~2 weeks before our observing run. Typical uncertainties on both spectra are of order 10–15%, so there may no (or not much) real differences between the two spectra near 12 μm. The red points are the disk-averaged flux densities of the images. The total width of the filters is indicated by the horizontal bars. (b) Disk-averaged Q band spectrum (solid black line), with superposed the disk-averaged values from the Q band images. The blue lines are results from Fletcher et al.'s (2014) forward model based upon the best-fitting Voyager/IRIS tropospheric temperature profile (dashed line), and a full retrieval of the Keck LWS data (solid line). (For interpretation of the references to color in this figure legend, the reader is referred to the web version of this article.)

much of the south polar enhancement (see Section 5 for a further discussion).

Neptune's total flux density was determined by taking the average of four measurements of that quantity[3]: the zero-spacing flux density from the visibility fit; the summed CLEAN components; the summed flux density in the image within a large box; and the summed flux density in the image within the planet diameter plus the restoring beam diameter. The average number is listed in Table 6; the uncertainty listed is based on the rms on the maps outside of Neptune (i.e., rms multiplied by $\sqrt{N}$, with N the number of beams on the disk) and the absolute calibration error mentioned above, in quadrature. The four separate estimates always agreed to within the uncertainty quoted. These flux densities were then converted to brightness temperatures using the full Planck equation and accounting for the cosmic background (CMB) radiation that is blocked by the planet, i.e., the CMB brightness temperature was added to that of the planet (see Appendix A for a full discussion). The flux densities and resulting brightness temperatures are summarized in Columns 2 and 3 of Table 6, respectively. Fig. 7 shows a

[3] See Kloosterman et al. (2008) for a detailed discussion of the various techniques for estimating the flux density from planetary radio interferometer measurements.

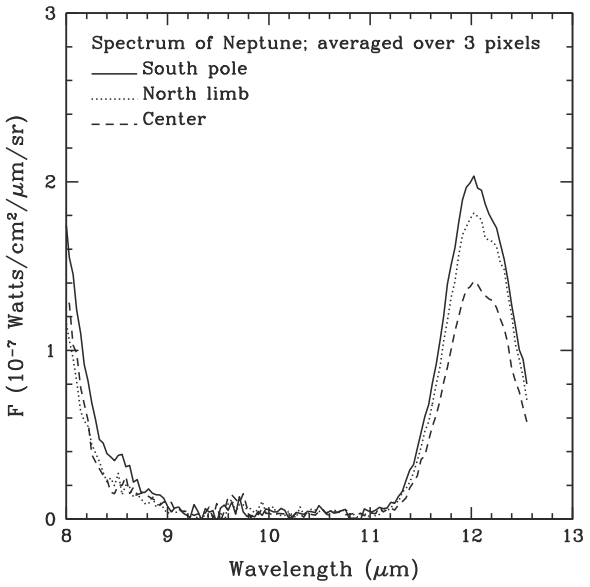

Fig. 5. N band spectra at 3 locations on Neptune's disk: we choose to show spectra at the two peak values along the slit, i.e., at the south pole and the north limb, as well as at the minimum, which is at the center of the disk.

radio spectrum of the planet, with our data points in red. We corrected all previously reported brightness temperatures for the CMB before plotting them, as discussed in Appendix A. (The model curves superposed on the data will be discussed in Section 5.2.) As shown, our disk-averaged brightness temperatures agree quite well with previous interferometric observations.

3. Data analysis: near-infrared wavelengths

At NIR wavelengths we detect sunlight scattered off clouds and aerosols in the upper troposphere and lower stratosphere. The images in Fig. 1, as discussed in Section 2.1, show that Neptune is usually characterized by latitudinal bands of cloud features, typically at southern midlatitudes between ~30°S and ~50°S, and similarly at northern midlatitudes between ~25°N and ~40°N. Relative to these midlatitudes, the equatorial region is usually quite cloudfree. In this paper we are primarily interested in Neptune's global circulation. Such patterns might be discerned at NIR wavelengths through a systematic study of the altitudes of individual cloud features. Altitudes are best determined by modelling spectra of cloud features using a radiative-transfer code, such as done by e.g., Roe et al. (2001), Sromovsky et al. (2001a, 2012), Gibbard et al. (2002, 2003), Karkoschka and Tomasko (2011), Irwin et al. (2011), Luszcz-Cook (2012) and Luszcz-Cook et al. (in preparation, 2014). Although we did not take spectra, on 6 October 2003 we imaged the planet through 5 narrow-band filters in addition to the broad-band J, H, and K′ filters. Since this represents a crude spectrum, we focus our analysis below on the 6 October data.

Before we delve into the analysis, Fig. 8 shows the filter transmission functions superposed on transmission profiles in Neptune's atmosphere. This gives the reader a sense of the sensitivity of our various filters to Neptune's atmospheric structure. The black, cyan and orange curves represent the depths to which 10%, 50% and 90% (respectively) of incident sunlight is transmitted (there and back, i.e., twice the pathlength). Panels a–d show curves for different model atmospheres to illustrate the dependence of these functions on the cloud/haze properties of the atmosphere. The model atmospheres are discussed in more detail in the subsections below. In Fig. 9 we show the corresponding contribution functions for each filter, calculated according to the algorithm described by Ádámkovics et al. (2006).

3.1. Cloud features

Fig. 10 shows our selection of cloud features, 17 in total, circled on each of the images. In order to determine the latitude, longitude and emission angle μ ($\mu = \cos\theta$, with θ the angle between the line of sight and the normal to the surface) of the features, each of the images was deprojected in a manner analogous to that used by e.g., Asay-Davis et al. (2009) and Lii et al. (2010). On the original (Fig. 10) images, a small subregion for each feature was extracted and viewed. In cases where the feature was distinct and easily identified, the position of the brightest feature pixel was used; the value at this location (peak I/F) was recorded, along with latitude, longitude and μ for that feature in a given filter. The latter three characteristics were determined from the deprojection. In some cases, a feature was not easily identified in one or several filters. Since we do need an estimate, or upper limit, for the I/F in these filters to help constrain the feature's altitude using our radiative-transfer (RT) code, we identified the likely location of the cloud on these images based on the feature's locations in other filters, and given the direction and magnitude of motion of the feature observed in the image sequence. The recorded I/F value for the feature in such filters is the mean value in this small region; a μ value is estimated from the μ values in the other filters. In Fig. 10, circles (solid lines) are centered on the adopted location of the peak I/F; for features that were not clearly detected, the circles are dashed.

Uncertainties in I/F were determined in the following way: for features which could be identified in a given filter, the error was set to be 20% of the I/F value to account both for photometry and filter-to-filter variations in Strehl ratio. In cases where features were not identified, the error is the straight sum of a 20% photometric error plus 2σ, where σ is the standard deviation of I/F over the region in which the mean I/F was taken. This additional error contribution accounts for the fact that the features were not actually detected above the background – the mean I/F of the region is therefore only a rough estimate of what the peak I/F of that feature

Table 5
Summary of microwave observations in 2003.

Wavelength (cm)	Frequency (GHz)	Band	Configuration	UT date (yr–mm–dd)	3C286[a] Jy	2131–121[b] Jy	Beam size (″)	Beam size (km)
0.7	43.34	Q	BnA	2003–10–12	1.55	2.33	0.16	3349
1.3	22.46	K	BnA	2003–10–11	2.57	2.54	0.30	6282
2.0	14.94	Ku	A	2003–06–26	3.48	3.36	0.32	6795
3.6	8.46	X	A	2003–06–27	5.21	3.99	0.44	9345
6.1	4.86	C	A	2003–06–28	7.48	3.87	0.75	15,936

Each track, including time on calibrators, was 8 h.
[a] Primary calibrator: adopted flux density.
[b] Secondary calibrator: derived flux density.

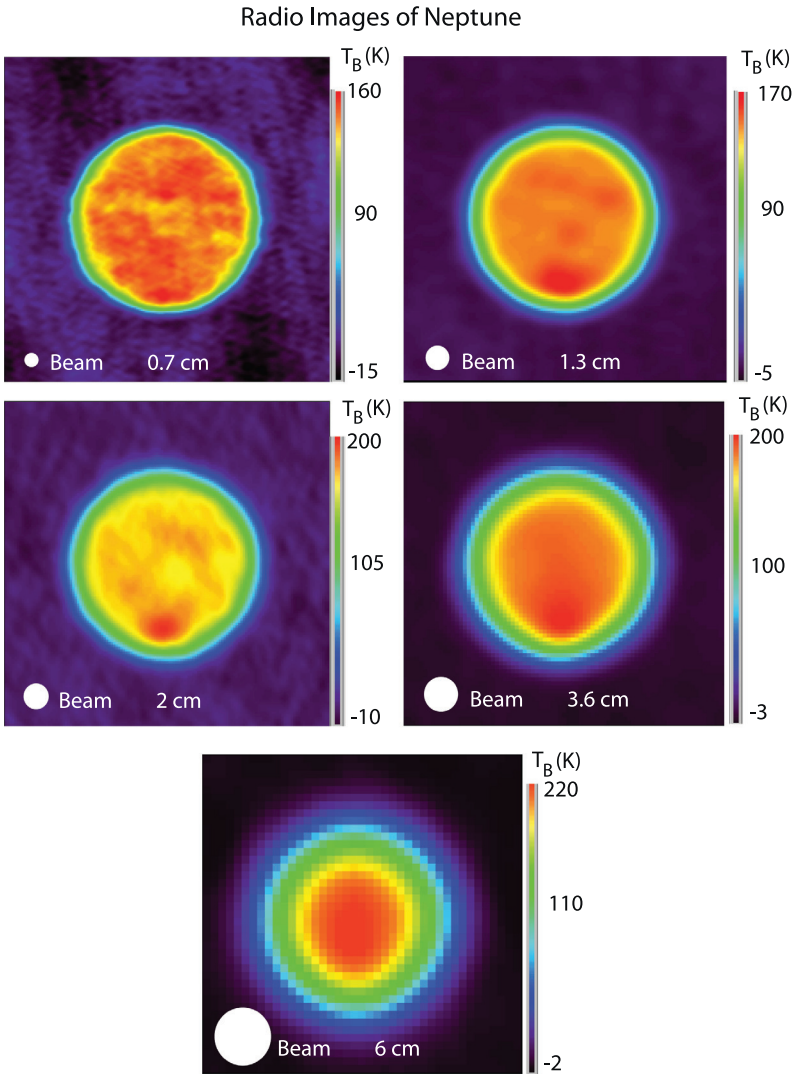

Fig. 6. VLA radio images of Neptune at all 5 wavelengths, as indicated. The intensity scale in units of brightness temperature is indicated on the right for each image, and the beam size (FWHM) is indicated in the lower left corner. Neptune has been rotated in these images so that its north pole is pointing up.

Table 6
Summary of observed and modeled microwave brightness temperatures.

Wavelength (cm)	Observed flux density (mJy)	Observed T_B[a] (K)	Nominal T_B[b] (K)	T_B including hot spot K
0.7	803.6 ± 40.3	147.4 ± 7.4	134.4	136.1
1.3	220.9 ± 11.1	150.6 ± 7.5	158.4	158.8
2.0	113.5 ± 3.4	169.7 ± 5.1	158.4	161.8
3.6	39.5 ± 1.2	183.3 ± 5.5	182.2	185.3
6.1	15.3 ± 0.46	215.1 ± 6.5	209.9	211.7

[a] Uncertainties are dominated by the absolute calibration, for which we adopted an error of 3% at 2–6 cm, and 5% at 0.7–1.3 cm.
[b] Disk-averaged brightness temperature for the nominal model (dry adiabat, enhancement in H_2S, H_2O, and CH_4 by a factor of ~50).

might be in that filter. The adopted values for I/F with uncertainties are recorded in Table 7.

For the purposes of spectral fitting, the μ value for each filter is used; that is, we incorporate into the fitting process the changes in viewing angle over the observing sequence. In Table 7, the median value of μ, (planetographic) latitude and longitude for the 8 observing filters is given for reference.

3.2. Radiative-transfer modeling at NIR wavelengths

We used a two-stream RT code at NIR wavelengths that was originally developed for Titan (e.g., Ádámkovics et al., 2009), and adapted to Neptune by Luszcz-Cook et al. (2010) and updated by Luszcz-Cook (2012). A total of 300 layers are distributed logarithmically from 20 bar to 10 μbar. The thermal profile is based on the MIR results described in Section 4 (see Fig. 14). At all three wavelength regimes we use the same thermal profile, and the same atmospheric composition. We adopted an atmospheric composition with volume mixing ratios of 0.15 for He and 0.003 for N_2 (Conrath et al., 1993). For CH_4 we used a deep mole fraction of 2.2% (Baines et al., 1995). At higher altitudes the methane abundance decreases towards the tropopause following the saturated vapor pressure curve with 100% relative humidity. Above the tropopause the CH_4 abundance rises to the stratospheric value of

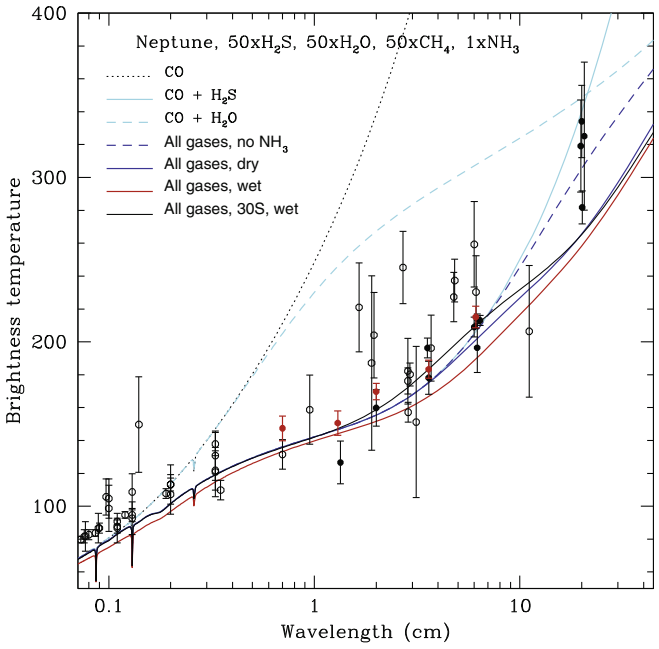

Fig. 7. Disk-averaged radio spectrum of Neptune, with superposed various model curves. The red points are the data presented in this paper; solid black points are older VLA data (de Pater et al., 1991, 1992), and the open circles are single dish data as compiled by de Pater and Richmond (1989). All data have been corrected for the cosmic background radiation. The models are described in the text (Section 5), and indicated in the legend. H_2 CIA has been included in all models. (For interpretation of the references to color in this figure legend, the reader is referred to the web version of this article.)

1.5×10^{-3} at 40 mbar (Lellouch et al., 2010) (see Fig. 14 for a visual representation of this profile). Gas opacity is dominated by H_2 collision-induced absorption (CIA: H_2–H_2, H_2–He, H_2–CH_4) and CH_4 opacity. For CIA, we use the coefficients for hydrogen, helium and methane from Borysow et al. (1985, 1988) and Borysow (1991, 1992, 1993), respectively, assuming an equilibrium ortho/para ratio for H_2. For methane, we use the correlated-*k* method. In choosing which of the published CH_4 coefficients to adopt, we follow the recommendations by Sromovsky et al. (2012) for outer planet NIR spectra. Rayleigh scattering is included as well, but is not important in this spectral region.

The data are well matched by models which assume there are two layers of scattering particles in the upper troposphere/stratosphere. We use an optically thick ($\tau = 10$) bottom cloud at all locations; the altitude of this cloud is set to 2.4 bar as in Irwin et al. (2011). The remaining properties of this cloud were determined by Luszcz-Cook (2012) by fitting the μ dependence of the spectrum in a dark part of Neptune's disk in field-integral spectroscopic (OSIRIS) data obtained at Keck. She found good fits using a value of 0.1 for the Henyey-Greenstein (HG) asymmetry parameter *g*, and a single scattering albedo of 0.3 at the wavelengths used in this paper (see also Luszcz-Cook et al., in preparation, 2014). The second layer is at higher altitudes. Since, as shown below, this layer has a lower optical depth than that of the bottom cloud for most situations, we refer to this layer as a "haze"; and unlike for the bottom cloud, we fit for the properties of this haze at each location by running a grid of models. The parameters that are varied across the grid are: particle size, single scattering albedo, bottom pressure of the cloud layer, and the optical depth at a wavelength of 1.6 μm. The optical depth is related to the particle number density at the bottom of this haze; this number density in our model falls off with altitude

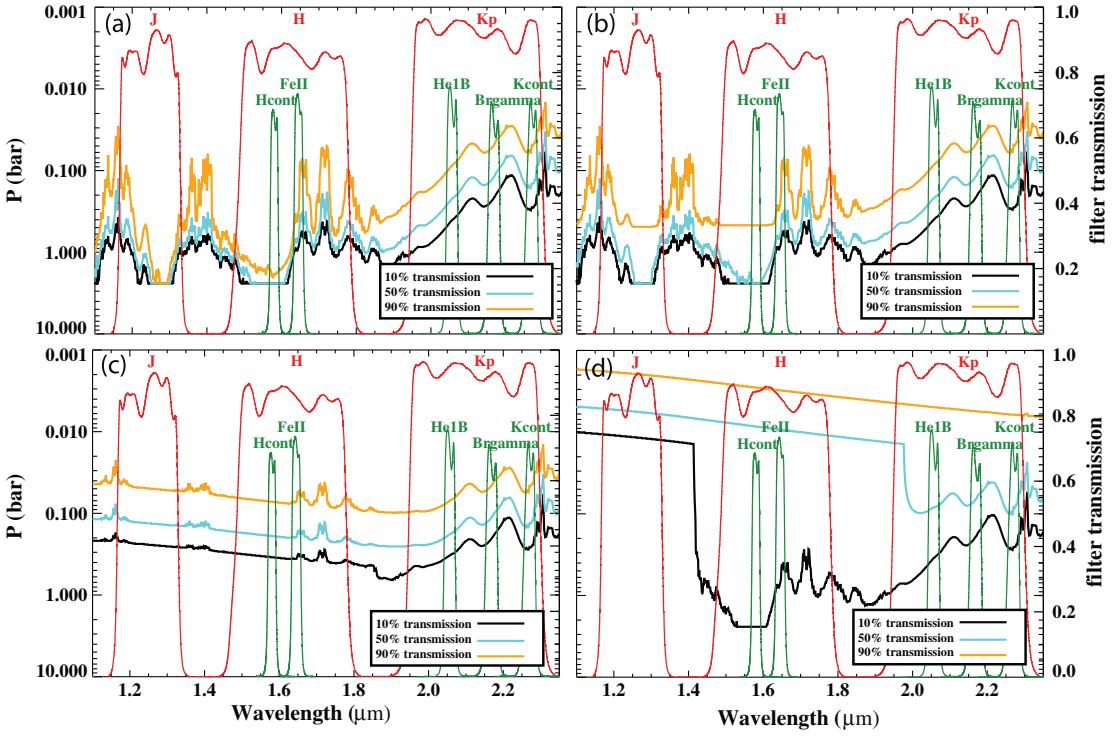

Fig. 8. NIR transmission functions for nadir ($\mu = 1$, disk center) viewing. On each panel, red and green curves indicate the filter transmission functions for the 3 broad-band (red) and 5 narrow-band (green) filters in the data set. The black, cyan and orange curves represent the depths to which 10%, 50% and 90% (respectively) of incident sunlight is transmitted (there and back, i.e., twice the pathlength through the atmosphere). These curves are shown for 4 different model atmospheres to illustrate the dependence of these functions on the cloud/haze properties. All atmospheric models have an optically thick cloud at 2.4 bar. The 'cutoff' observed at 2.4 bar on each panel is due to this bottom cloud. (a) Atmospheric model without additional hazes. (b) Atmosphere with an additional optically thin haze (or cloud) at 0.9 bar. (c) A model that is roughly matched to the fitted properties of cloud feature #2: an optically thick ($\tau = 2$ at 1.6 μm) cloud has been added at 0.44 bar ($r_p = 0.1$ μm and $\varpi = 0.4$). (d) A model that is roughly matched to the fitted properties of feature #17: a cloud with an optical depth of 0.6 at 1.6 μm has been added at 0.014 bar ($r_p = 0.1$ μm and $\varpi = 0.7$). (For interpretation of the references to color in this figure legend, the reader is referred to the web version of this article.)

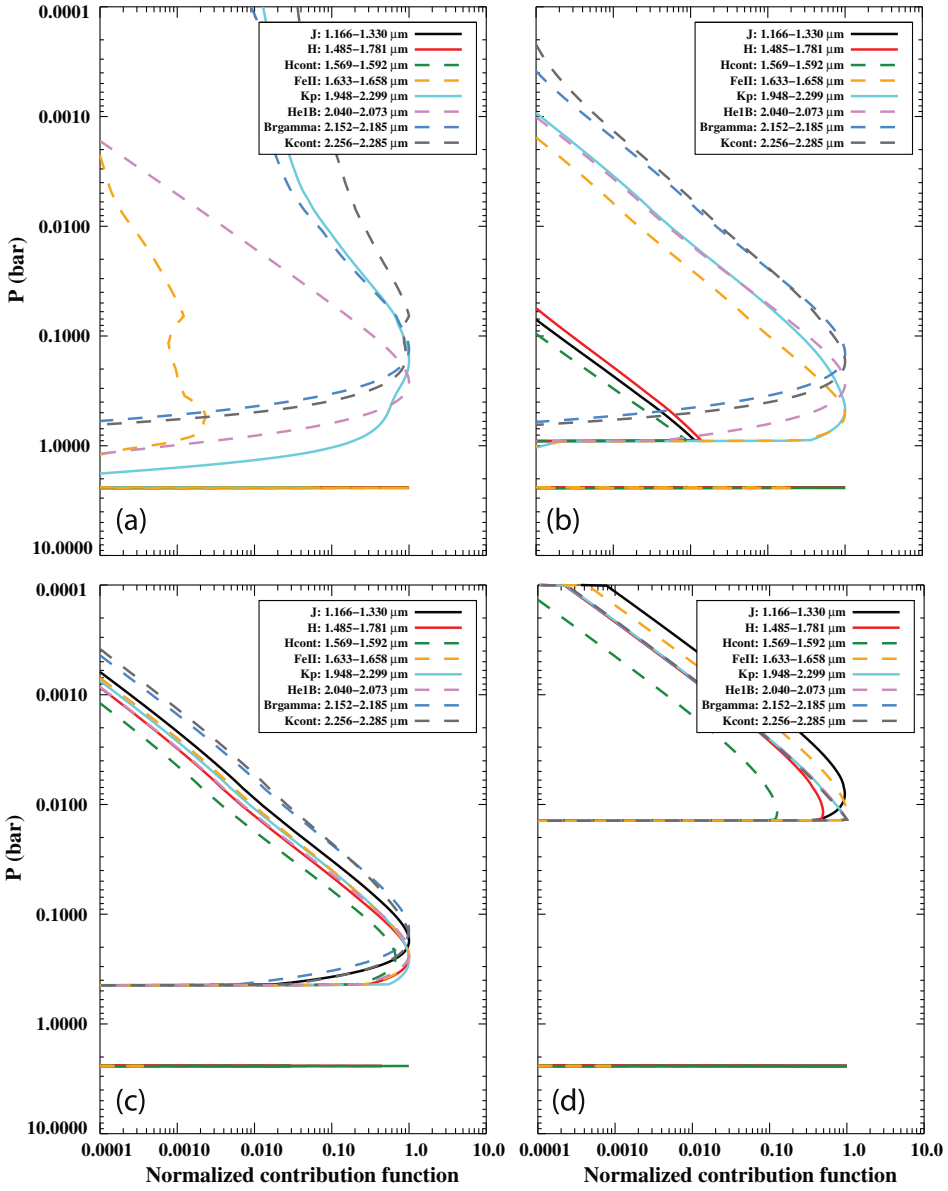

Fig. 9. NIR contribution functions for the same four models as in Fig. 8. Each curve shows the average contribution over the specified filter. The details of the four models are described in Fig. 8.

with a scale height equal to 0.5 times the pressure scale height of the gas.

We treat particles in this haze layer as Mie scatterers, with a size distribution analogous to that found on Titan (Mitchell et al., 2011):

$$N(r) \propto r^6 \exp(-6r/r_p), \quad (2)$$

where $N(r)$ is the number density of particles of radius r and r_p is the radius at which the number density is largest. The dielectric constant was set to 1.4, with an imaginary part equal to zero (Luszcz-Cook et al., 2010). We ran models with $r_p = 0.1$, 0.5 and 1.0 μm. The extinction cross section and Henyey-Greenstein asymmetry parameter of the scattering are calculated using Mie theory. The single scattering albedo (ϖ) of the haze is run for 13 values between 0.28 to 1.0 in linear steps.

The bottom pressure (P_{max}) of the haze layer is varied from 2.4 bar (i.e., at the location of the bottom cloud) to 2 mbar in 15 steps. The optical depth is varied from 0.05 to 50; the (logarithmic) step size is varied over this range so that the incremental change between models is roughly uniform (we use more steps between 0.35 and 7 because changes in τ over this part of the range are more significant).

We run this grid of models at 14 μ values from 0.31 to 1.0, which is the range of μ values for the features identified in the data. The step size for μ is varied (logarithmic) to keep the incremental change between models roughly uniform.

After running and saving this rough grid of models, the corresponding filter I/F for each of the 8 filters for each model in the grid is calculated by multiplying the data by the filter transmission function and integrating. The filter transmission functions were taken from the NIRC2 documentation,[4] with two caveats: the filter transmission functions for all of the narrow-band filters were shifted so that they are centered between the 'cut-on' and 'cut-off' filter values quoted in the NIRC2 documentation; and the BrGamma filter function was also stretched so that the band half power points

[4] https://www2.keck.hawaii.edu/inst/nirc2/filters.html.

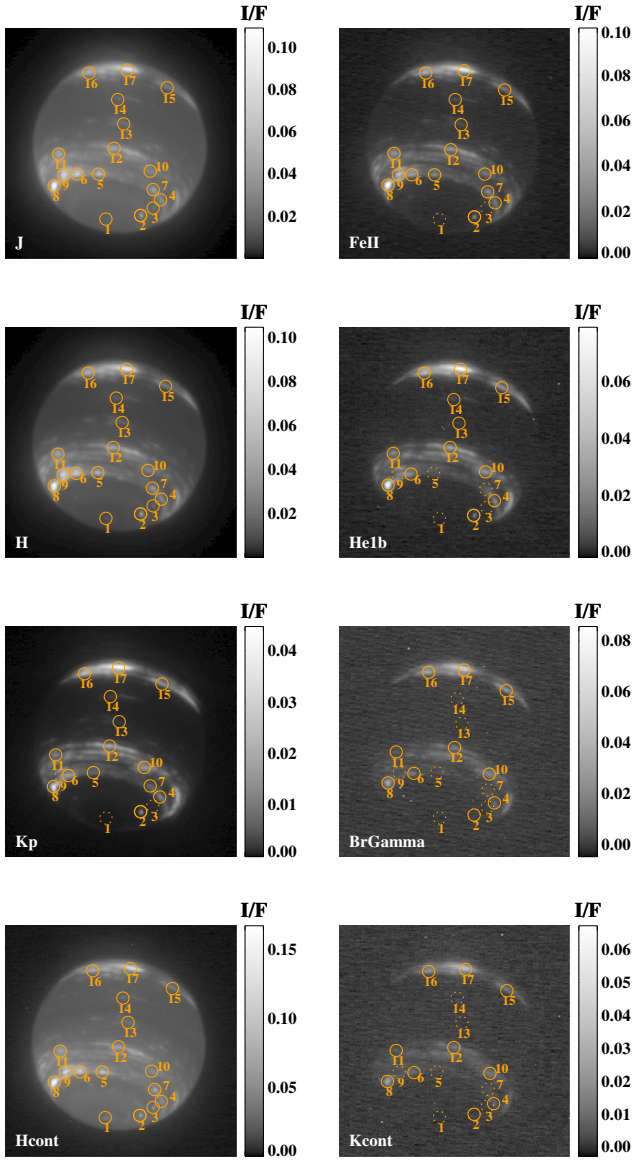

Fig. 10. Locations of the cloud features modeled at NIR wavelengths. The features are arranged as a function of latitude, from the south pole (# 1) to the north. Circles are centered on the adopted location of the peak I/F (solid) or, for features that were not clearly detected, on the center pixel value of the estimated feature location (dashed). The features are indicated on each of the broad- and narrow-band images used in the RT models. The images are arranged from short to long wavelengths, starting with the three broad-band filters, and then the five narrow-band filters.

match these 'cut-on' and 'cut-off' values (J. Lyke and H. Tran, private communication, 2013).

After interpolating the calculated filter I/Fs onto a much finer grid, we selected for each data value of I/F (for each feature and for each filter) those models with the μ value closest to the data value, and compared these to the data. Our best-fit models to each of the 17 features are shown in Fig. 11. In most cases, excellent fits are obtained; for a few features, notably features 5 and 8, the models are not consistent with the data at the level of the adopted uncertainties.

3.3. NIR results

In Fig. 11 we show the entire model spectrum along with the data (crosses with errorbars; the diamonds show the model values for the specific wavelength/filter). On each panel, the values for the free parameters of the haze layer are listed. As shown, all 4 parameters (optical depth τ, the bottom pressure of the haze layer P_{max}, particle radius r_p and single scattering albedo ϖ) usually differ from feature to feature. In this paper we are particularly interested in the altitude (or pressure) of the cloud feature, since this parameter is most relevant to our overarching goal of constraining Neptune's global atmospheric circulation. To better judge our derived altitudes, we calculate the quantity χ^2 for each feature n, as a function of r_p, P_{max}, τ, and ϖ in the following way:

$$\chi^2[n, r_p, P_{max}, \tau, \varpi] = \sum_i \frac{((I/F)_d[n,i] - (I/F)_m[n,i,r_p,P_{max},\tau,\varpi])^2}{(err[n,i])^2}, \quad (3)$$

where we sum over the filters, i. The subscripts d and m stand for data and model, respectively. The quantity err is the uncertainty for each I/F value, as discussed above. For each feature, we find a 2-dimensional (2D) χ^2 surface: for each P_{max} and τ we find the minimum χ^2 solution (regardless of particle size or ϖ), and plot this χ^2 value as a function of P_{max} and τ in Fig. 12. The green contour indicates the 1σ uncertainties of $[\tau, P_{max}]$ together (defined as where $\chi^2 - min(\chi^2) \equiv \Delta\chi^2 = 2.3$, the 1-$\sigma$ [68.3% of points enclosed] value for a χ^2 distribution with 2 free parameters). The orange contour indicates $\Delta\chi^2 = 1.0$, and the vertical and horizontal projections of that contour (dashed lines) indicate the 1σ uncertainties of P_{max} and τ when considered independently (that is, without regard to the other parameter). The best fit P_{max} and τ values, along with the minimum and maximum values found from the 2D χ^2 surfaces, are given in Table 8.

From Fig. 12 and Table 8 we find, in essence, three different layers of cloud features: (i) Features at pressures $P_{max} > 1$ bar. Three of the features we investigated are located at these deep levels. The feature at the south pole (#1) is the deepest of these, at ~2 bar. Features 3 and 9 are also deep, at ~1 and 1.6 bar, respectively. In fact, even a cursory examination of the images shows that these features must be deep in the atmosphere, since there is essentially no trace of these clouds in the broad-band K′ filter, which is sensitive to relatively high altitudes (see Figs. 8 and 9). Features 1 and 3 are also absent in the FeII filter, which is characterized by strong methane absorption, although not as strong as in the 2-μm band. Interestingly enough, feature 9 is visible in the FeII band, which has been attributed to an extremely high optical depth of this feature (Table 8). (ii) Features at pressures $P_{max} \sim 0.2$–0.6 bar. Several of the ~0.5 bar features are at southern midlatitudes (#5, #7 at ~50°S), and one (#2) can be characterized as a South Polar Feature (SPF). The two equatorial features (#13, #14) are at the high end of this pressure range, at ~0.25–0.35 bar. None of these features is seen in the narrow-band 2-μm filters. (iii) Features at pressures $P_{max} < 0.05$ bar; these features are located in the stratosphere. All features at northern midlatitudes (~30°N) are close to 10 mbar. All other stratospheric features are at southern midlatitudes (~30–50°S), at altitudes near 20–30 mbar. These features, being high up in the atmosphere, are visible through all filters.

With these models in mind, we return to Figs. 8 and 9, where atmospheric transmission and filter contribution curves are shown for various models. In all panels of both figures atmospheric opacity is provided by the gas (Section 3.2), together with an optically thick cloud at 2.4 bar; the effect of this cloud is shown by the flat transmission curves at that level in Fig. 8, and by the single horizontal line at 2.4 bar in Fig. 9. The model in Figs. 8a and 9a have no additional opacity. Those in Figs. 8b and 9b have an additional haze layer at 0.9 bar (i.e., $P_{max} = 0.9$ bar). Figs. 8c and 9c show results for an atmosphere that most closely resembles our model of cloud feature 2, and in Figs. 8d and 9d the atmosphere is similar to that of cloud feature 17. The combination of these four panels in

Table 7
NIR cloud feature characteristics.

Feature	μ	latitude (°)	longitude (°)	I/F J	I/F H	I/F Kp	I/F Hcont	I/F FeII	I/F He1b	I/F BrGamma	I/F Kcont
1	0.50	−88.8	347.1	0.019 ± 0.004	0.013 ± 0.003	0.0005 ± 0.0002	0.039 ± 0.008	0.003 ± 0.001	0.0011 ± 0.0008	0.000 ± 0.001	0.001 ± 0.001
2	0.55	−66.5	232.7	0.042 ± 0.008	0.039 ± 0.008	0.012 ± 0.002	0.06 ± 0.01	0.027 ± 0.005	0.016 ± 0.003	0.002 ± 0.002	0.003 ± 0.002
3	0.59	−56.4	239.1	0.022 ± 0.004	0.018 ± 0.004	0.0013 ± 0.0003	0.06 ± 0.01	0.005 ± 0.002	0.002 ± 0.001	0.002 ± 0.002	0.002 ± 0.001
4	0.62	−49.8	241.0	0.034 ± 0.007	0.031 ± 0.006	0.012 ± 0.002	0.05 ± 0.01	0.022 ± 0.004	0.021 ± 0.004	0.013 ± 0.003	0.011 ± 0.002
5	0.92	−48.8	321.4	0.06 ± 0.01	0.05 ± 0.01	0.008 ± 0.002	0.10 ± 0.02	0.030 ± 0.006	0.008 ± 0.002	0.005 ± 0.002	0.003 ± 0.002
6	0.80	−48.4	347.0	0.07 ± 0.01	0.06 ± 0.01	0.016 ± 0.003	0.11 ± 0.02	0.039 ± 0.008	0.022 ± 0.004	0.019 ± 0.004	0.010 ± 0.002
7	0.78	−48.2	261.4	0.044 ± 0.009	0.039 ± 0.008	0.008 ± 0.002	0.07 ± 0.01	0.031 ± 0.006	0.009 ± 0.003	0.004 ± 0.002	0.005 ± 0.002
8	0.45	−46.8	27.5	0.11 ± 0.02	0.10 ± 0.02	0.037 ± 0.007	0.17 ± 0.03	0.10 ± 0.02	0.08 ± 0.02	0.037 ± 0.007	0.028 ± 0.006
9	0.68	−45.9	3.8	0.08 ± 0.02	0.07 ± 0.01	0.014 ± 0.004	0.12 ± 0.02	0.06 ± 0.01	0.018 ± 0.005	0.006 ± 0.002	0.005 ± 0.002
10	0.88	−38.5	273.7	0.031 ± 0.006	0.028 ± 0.006	0.015 ± 0.003	0.05 ± 0.01	0.022 ± 0.004	0.026 ± 0.005	0.023 ± 0.005	0.015 ± 0.003
11	0.70	−31.5	358.1	0.045 ± 0.009	0.042 ± 0.008	0.012 ± 0.002	0.07 ± 0.01	0.035 ± 0.007	0.023 ± 0.005	0.011 ± 0.002	0.010 ± 0.002
12	0.10	−30.2	309.1	0.044 ± 0.009	0.042 ± 0.008	0.019 ± 0.004	0.07 ± 0.01	0.035 ± 0.007	0.033 ± 0.007	0.019 ± 0.004	0.016 ± 0.003
13	0.96	−12.8	305.2	0.022 ± 0.004	0.016 ± 0.003	0.0022 ± 0.0004	0.037 ± 0.007	0.010 ± 0.002	0.0047 ± 0.0009	0.001 ± 0.001	0.002 ± 0.001
14	0.83	4.5	312.4	0.021 ± 0.004	0.015 ± 0.003	0.0031 ± 0.0006	0.033 ± 0.007	0.010 ± 0.002	0.006 ± 0.001	0.002 ± 0.002	0.002 ± 0.002
15	0.46	27.8	277.0	0.026 ± 0.005	0.023 ± 0.005	0.014 ± 0.003	0.040 ± 0.008	0.021 ± 0.004	0.024 ± 0.005	0.027 ± 0.005	0.015 ± 0.003
16	0.35	31.5	342.6	0.05 ± 0.01	0.048 ± 0.001	0.024 ± 0.005	0.07 ± 0.01	0.046 ± 0.009	0.043 ± 0.009	0.035 ± 0.007	0.021 ± 0.004
17	0.42	36.4	312.7	0.09 ± 0.02	0.08 ± 0.02	0.045 ± 0.009	0.13 ± 0.03	0.09 ± 0.02	0.08 ± 0.02	0.06 ± 0.01	0.039 ± 0.008

The cosine of the emission angle (μ), (planetographic) latitude, and longitude are the medians for the features in each set of 8 filter images. I/F is the peak I/F for the feature in the specified filter; in cases where the feature could not be identified, the quoted I/F is the mean in a region where the feature is expected to be. Uncertainties are estimated as 20% of I/F, from uncertainty in the photometry; if feature was not clearly identified, then the error is calculated as the sum of a 20% photometric error plus twice the standard deviation of the region in which I/F was calculated.

Figs. 8 and 9 clearly show how contribution functions depend on the models.

The altitudes we derived for these 17 features are not inconsistent with those determined previously (e.g., Roe et al., 2001; Sromovsky et al., 2001a; Gibbard et al., 2003; Karkoschka and Tomasko, 2011; Irwin et al., 2011; Luszcz-Cook, 2012; Luszcz-Cook et al., in preparation, 2014), although the details do differ somewhat. We all find that the clouds near the equator are in the upper troposphere, at a few tenths of a bar (Irwin et al., 2011; Luszcz-Cook, 2012; Luszcz-Cook et al., in preparation, 2014). For other features the various authors do find differences in altitudes, however. This may be caused by slightly different model-atmosphere assumptions and gas opacity parameters, choice of stratospheric CH_4 abundance (Irwin et al., 2011 evaluate the effect of changes in the stratospheric CH_4 abundance on cloud altitude), and by differences in the observed spectral windows. For example, Irwin et al. consider only H band spectra, and they vary the optical depth of both the bottom and upper clouds. We have a fixed bottom cloud, and we consider discrete filters in both the H and K band wavelength regimes. Gibbard et al. consider spectra over only the K band, and both they and Roe et al. use a gas-only model with one simple reflecting layer to deduce the cloud altitudes. Karkoschka and Tomasko utilized HST/STIS spectroscopic measurements in the 300–1000 nm wavelength range. Luszcz-Cook (2012) and Luszcz-Cook et al. (in preparation, 2014) consider spectra over both the H and K band windows, which improves their ability to determine the altitudes of the highest cloud features. Given the differences between observations and model assumptions, it is surprising (and comforting), that the various authors reached more or less similar conclusions.

As in essentially all previous works, we see the deepest clouds at far southern latitudes, and the highest at northern midlatitudes. We note here that Karkoschka and Tomasko (2011) determined a methane mixing ratio of 4 ± 1% at pressure levels $P > 3.3$ bar, and they show that the methane abundance in Neptune's troposphere is about a factor of 3 lower at high southern latitudes compared to low latitudes, down to at least the ~3 bar level. If we would have used a higher methane abundance, our derived cloud pressures would have been somewhat lower.

What is striking, however, is that at certain latitudes in the southern midlatitude range we see clouds in the stratosphere next to clouds in the troposphere. Hence, cloud activity at southern midlatitudes appears to happen at two levels: one in the stratosphere, at ~0.02–0.03 bar level, and one in the troposphere at altitudes below the 0.3 bar level; best-fit pressures for the tropospheric cloud level in our data range from ~0.5 bar down to 1.6 bar. Fry and Sromovsky (2004), in a DPS poster, also showed evidence of different cloud altitudes at the same latitude, though no further details were provided. Luszcz-Cook (2012) examined clouds in images obtained with the integral-field spectrograph OSIRIS on the Keck telescope, and shows evidence of the same. She modeled the clouds with a tropospheric haze (~0.5 bar) and one in the stratosphere (~80 mbar), not unlike our two haze layers. We show that clouds at the same latitude apparently can vary in altitude by as much as 80 km, or of order 4 scale heights. This could perhaps play a role in the wind dispersion measured on Neptune by e.g., Limaye and Sromovsky (1991), Sromovsky et al. (2001a,b), Martin et al. (2012), and Fitzpatrick et al. (2013). A difference in cloud location by 4 scale heights could lead to a dispersion in wind velocity of order 100 m/s, given the near-maximum vertical wind shear of ~30 m/s per scale height as suggested by Conrath et al. (1989) based on Voyager IRIS observations. However, some of the authors report even higher values for the observed velocity dispersion, while the highest wind shear in the Voyager data was measured at low latitudes. At southern midlatitudes – where we observe cloud altitudes to span of order 4 scale heights – the vertical wind shear in the Voyager data was close to zero. Similarly, Fletcher et al. (2014) also show a near-zero vertical wind shear at southern midlatitudes based on the MIR 2003 data presented in this paper.

In terms of overall dynamics, one would expect a general rising of air at latitudes where we see an abundance of clouds, and subsiding air at latitudes where clouds are mostly absent. However, we should bear in mind that in addition to these large-scale regions of rising and sinking motions, there are apt to be small localized regions of rising plumes due to convective storms and localized upwellings due to anticyclonic vortices (i.e., local "weather"), as discussed further in Section 6.

4. Data analysis: mid-infrared wavelengths

At MIR wavelengths we detect thermal emission from the stratosphere (~0.1 mbar) down to the upper troposphere

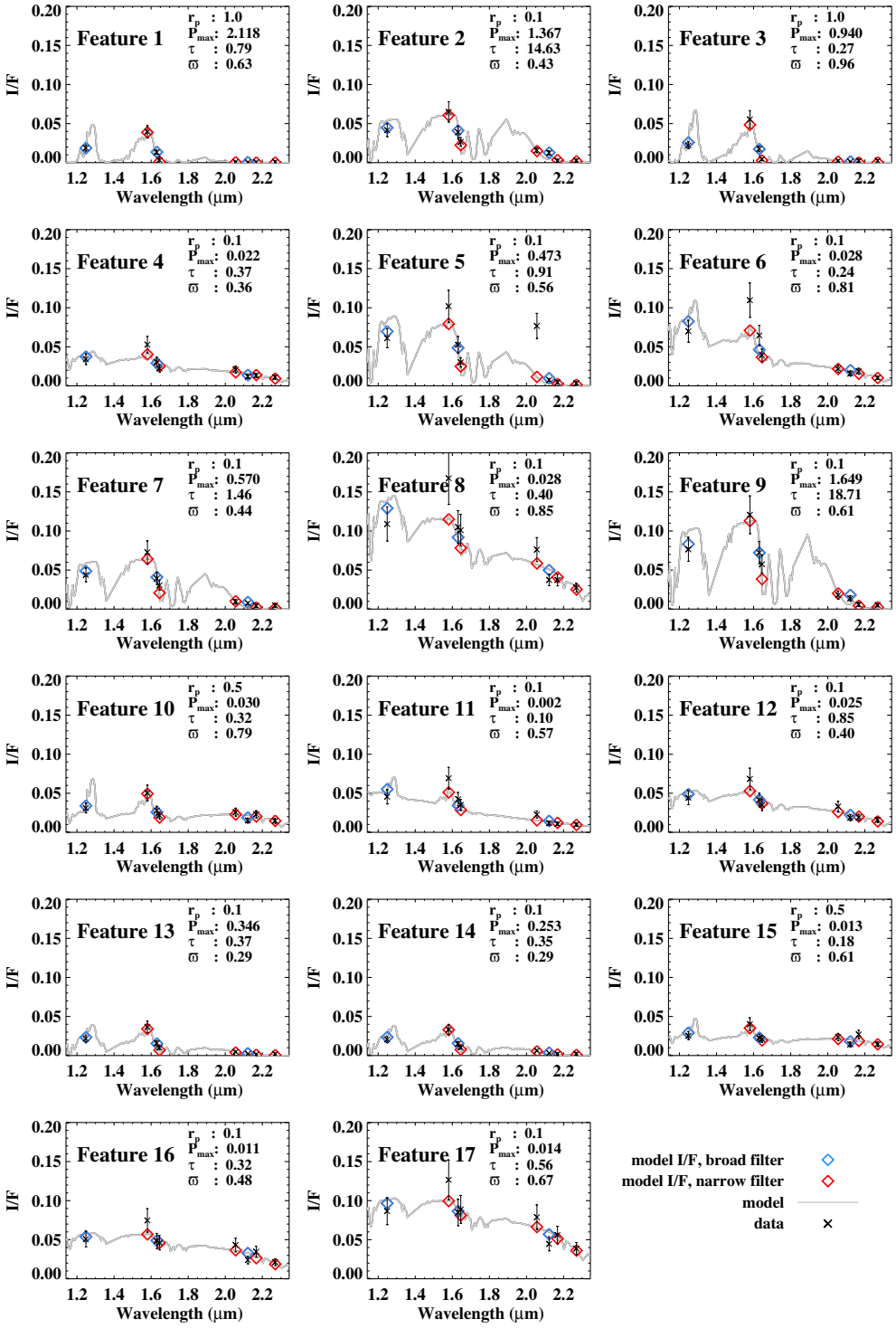

Fig. 11. Our best fit to the NIR filter I/F values of 6 October 2003. Data are shown in black, with error bars. Diamond symbols are model I/F values, with broad filters in blue and narrow-band filters in red. For reference, a corresponding model spectrum (which uses an average value of μ) is shown in grey. (For interpretation of the references to color in this figure legend, the reader is referred to the web version of this article.)

(~200 mbar), as shown by the contribution functions in Fig. 13. The altitude range probed in a given filter is determined by the atmospheric opacity in that filter. Collision-induced absorption by hydrogen (CIA) is the dominant source of opacity; several hydrocarbons contribute to the opacity at specific wavelengths/filters, as summarized in Table 3. Opacity due to aerosols was ignored, since the particles measured in the NIR are too small to have an effect on the MIR. Since the observed brightness temperature depends on molecular gas opacity as well as on the atmospheric temperature structure, it is not possible to uniquely determine the temperature and gas abundance from a single filter. However, with the set of 8 filters, plus N and Q band spectra, we can begin to disentangle the various contributions to each filter.

The images and spectra presented in this article were analysed in detail by Fletcher et al. (2014) as part of their comparison of solstice-era datasets to the Voyager infrared observations.

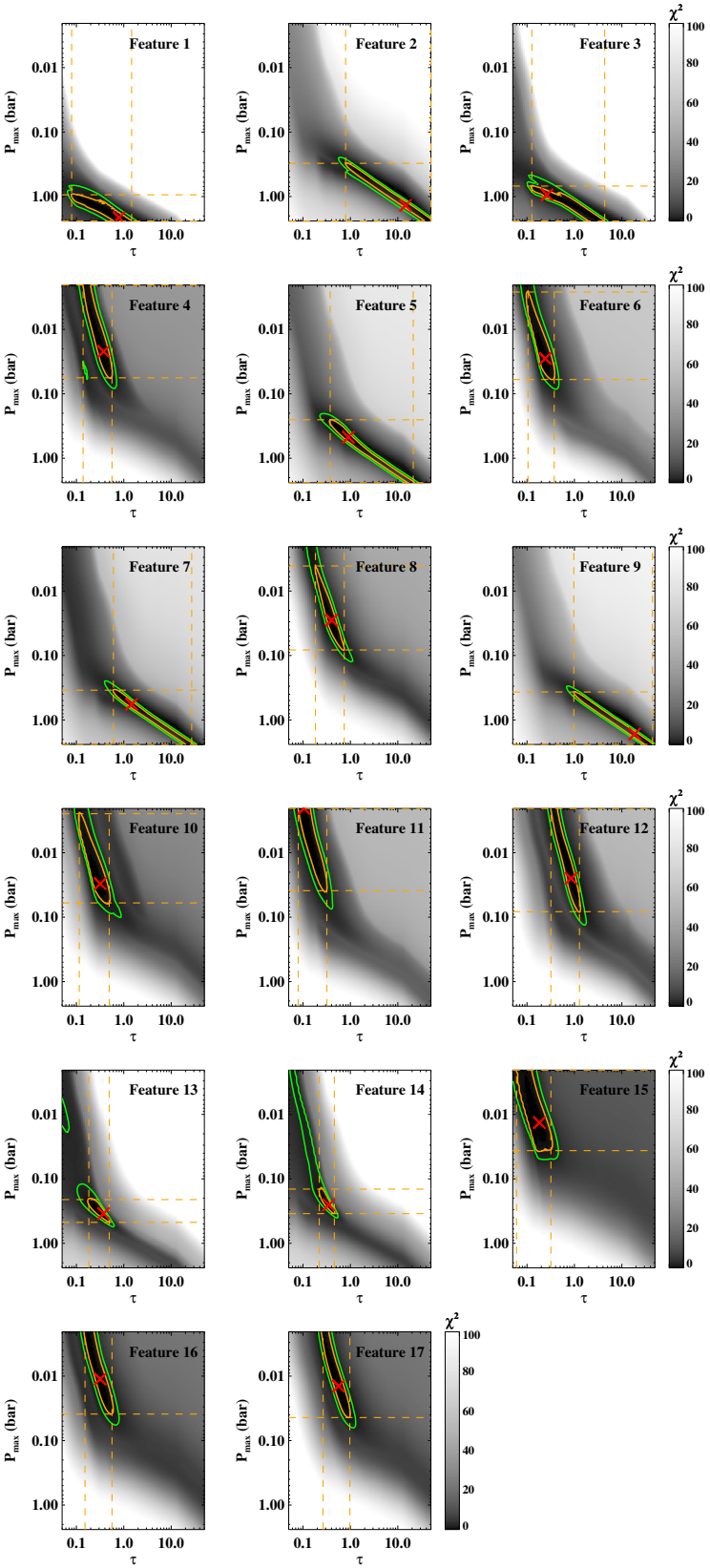

Fig. 12. χ^2 surfaces for the 17 features modeled in the NIR; shading indicates the value of χ^2 for a given $[P_{max}, \tau]$. The red X indicates the location of the best fit. The green contour is the combined 1σ contour (at $\Delta\chi^2 = 2.3$). The orange contour defines $\Delta\chi^2 = 1.0$, and the dashed orange lines are the projections of this orange contour onto the *x* and *y* axes. These projections indicate the 1σ uncertainties for the two parameters independently. (For interpretation of the references to color in this figure legend, the reader is referred to the web version of this article.)

Table 8
Best-fit bottom pressure and optical depth for selected NIR features.

Feature number	Latitude (°)	Best-fit pressure (bar)	Min pressure (bar)	Max pressure (bar)	Best-fit τ	Min τ	Max τ
1	−88.8	2.1	0.94	2.4	0.8	0.08	1.
2	−66.5	0.44	0.27	2.4	2.	0.7	50
3	−56.4	0.94	0.69	2.4	0.3	0.1	4.
4	−49.8	0.022	0.0021	0.056	0.4	0.1	0.6
5	−48.8	0.47	0.25	2.4	0.9	0.4	20
6	−48.4	0.028	0.0026	0.060	0.2	0.1	0.4
7	−48.2	0.57	0.35	2.4	1.	0.6	30
8	−46.8	0.028	0.0041	0.082	0.4	0.2	0.7
9	−45.9	1.6	0.37	2.4	20	0.1	40
10	−38.5	0.030	0.0021	0.060	0.3	0.1	0.5
11	−31.5	0.0021	0.0021	0.039	0.1	0.08	0.3
12	−30.2	0.025	0.0021	0.082	0.8	0.3	1.
13	−12.8	0.35	0.21	0.47	0.4	0.2	0.5
14	4.5	0.25	0.14	0.35	0.3	0.2	0.5
15	27.8	0.013	0.0021	0.036	0.2	0.06	0.3
16	31.5	0.011	0.0025	0.039	0.3	0.2	0.6
17	36.4	0.014	0.0021	0.044	0.6	0.3	0.1

Best-fit bottom pressure and optical depth for selected NIR features, from the grid of models. The minimum and maximum pressure values that were modeled were 0.0021 bar and 2.4 bar, respectively; the minimum and maximum optical depth values modeled were 0.05 and 50, respectively.

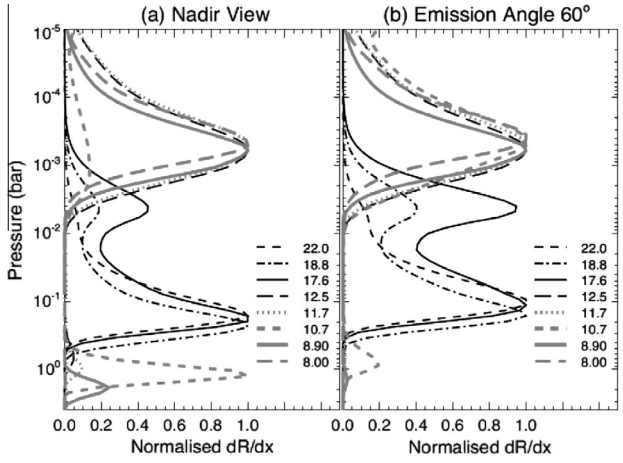

Fig. 13. Contribution functions for the MIR filters at two different emission angles (nadir and 60°). The filters are indicated in the legend. These functions are based on our best-fit profiles, discussed in Section 4. Note how the sensitivity changes from nadir to near the limb, including the secondary stratospheric peak for 17–19 μm filters, and the diminishing importance of the 1-bar sensitivity of the 10.7 μm filter (from Fletcher et al., 2014).

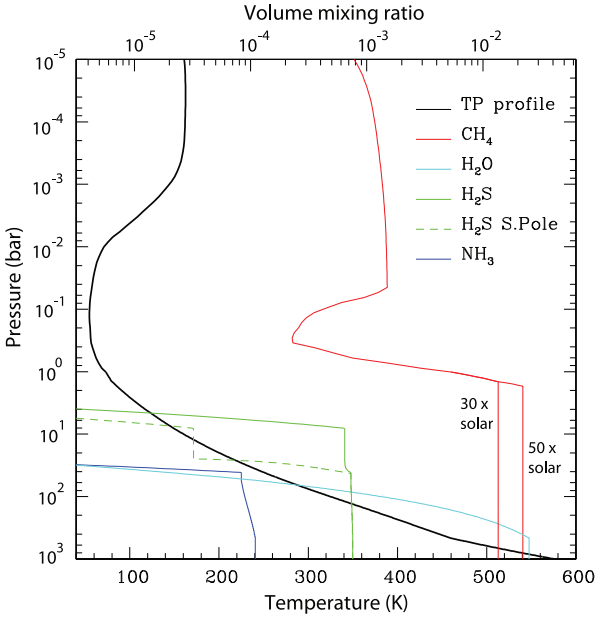

Fig. 14. Temperature–pressure profile (black line) as derived from the MIR N band spectrum in the stratosphere and the Q band spectrum in the troposphere, at pressures ~200 mbar. At deeper levels (higher pressures) the profile is extrapolated according to a wet adiabat (see Section 5, nominal model), assuming a composition of Neptune's deep atmosphere where CH_4, H_2S and H_2O are enhanced by a factor of 30 above the protosolar C, S and O values, and NH_3 is equal to the solar N value. The abundance profiles of these species are indicated by the colored lines. All profiles, except for CH_4, follow the saturated vapor curves above their condensation temperatures (including the solution and NH_4SH clouds). At NIR and MIR wavelengths we used a deep CH_4 abundance of 2.2% (50× the protosolar C abundance), as indicated. At radio wavelengths the deep abundance was 1.35% (30× the protosolar abundance). The dashed line shows the abundance profile for H_2S that best fits Neptune's south polar region, as described in Section 5.

Their analysis used the suite of radiative transfer and retrieval software known as NEMESIS (Irwin et al., 2008). We refer the reader to Fletcher et al. for a complete discussion of the data analysis approach and limitations, but summarise the main points here.

The reference atmospheric profiles for all gases, including methane (shown in Fig. 14) and hydrocarbons, along with the sources of spectral line data, are described in Fletcher et al. The 2003 MIR data were analysed in a multi-step process to ensure an accurate comparison to Voyager-era observations. The latitudinally-resolved N-band (8–13 μm) spectra were used to derive the stratospheric temperature and ethane abundance. The disk-averaged Q band (18–22 μm) spectrum was used to determine the temperature in Neptune's troposphere. Fletcher et al. (2014) also used Voyager-era tropospheric temperatures to simulate the expected Q-band spectrum using the geometry of the 2003 Keck observations and integrating over the disk. The Voyager brightness was found to be consistent with the Keck brightness temperature spectrum to within 0.7 K. The resulting temperature–pressure profile is plotted in Fig. 14; this profile is also used in our NIR and radio data modeling (see Section 5.1 for details on the extrapolation of this curve to pressures $\gtrsim 1$ bar). The globally-averaged ethane abundance derived from fitting the 12.3 μm emission feature is 767^{+122}_{-163} ppb at 1 mbar. The ethane abundance is highly sensitive to the derived stratospheric temperature profile, with small discrepancies leading to large systematic offsets in ethane. Fletcher et al. discuss the caveats associated with this abundance, including the lack of constraint on the stratospheric temperature profile and the possibility of terrestrial ice cloud contamination in the 12-μm region.

With the stratospheric and tropospheric temperatures and ethane abundance determined from the Keck spectroscopy, the second stage of this analysis concerned the imaging. To demonstrate the vertical sensitivity of the suite of eight filters, we show the contribution functions for each filter in Fig. 13. Contribution functions show greatest sensitivity at several different pressure levels, which introduces a degeneracy in their interpretation. Moreover, Neptune's south pole is observed at high emission angles, where the contribution functions are shifted to higher altitudes. For the Q-band filters, the small 3–6 mbar contributions are quite pronounced at high emission angles, while the 8—9 μm methane band filter contributions near 1 bar have almost disappeared at these emission angles. Only the sensitivity of the 22-μm filter remains concentrated near the tropopause. Hence the degeneracy observed in the contribution functions of these images implies our capabilities for studying tropospheric temperatures are limited.

Fletcher et al. (2014) stacked the MIR images to create an 8-image data cube (i.e., with wavelength along the third axis) to retrieve the physical temperature at different locations on Neptune's disk. Because the 17.65- and 18.75-μm filters are increasingly more sensitive to the stratosphere at the 1–10 mbar levels at higher emission angles (Fig. 13), it is not immediately clear whether the bright polar emission originates in the troposphere and/or stratosphere. The same is true for the 8—11 μm filters, which are sensitive to altitudes both near the 1 bar and the 0.1–1 mbar levels. The 22-μm image, however, partially breaks this degeneracy, and suggests that the warm pole must also extend into the troposphere at the 100–200 mbar region. Indeed, Fletcher et al. (2014) show through simulations that the physical temperature at the south pole is higher than at mid-latitudes from the 0.1–1 mbar level in the stratosphere all the way down to the tropopause region.

Fig. 15 shows the final MIR results, where contours of physical temperature are plotted as a function of pressure and planetocentric latitude. The uncertainty on the temperatures shown in Fig. 15 arise from several sources: (i) random pixel-to-pixel uncertainty that was estimated from the sky background on each image; (ii) systematic radiometric uncertainty that we quantify to be ±10%; and (iii) uncertainties related to the retrieval process, such as the level of vertical smoothing applied to the temperature profile (a technique used to reduce the number of free parameters in the retrieval, e.g., Irwin et al., 2008). Random uncertainties are estimated to be 1–2 K in the troposphere, increasing to 2–4 K in the mid-stratosphere. Contributions from (ii) and (iii) are systematic (i.e., affecting all latitudes) and so do not add uncertainty to the relative errors on the zonal mean. They do add 4–8 K uncertainties to the absolute errors. Ignoring the northern and southern edges of the domain, which are plagued by spurious effects, we see that the temperature is remarkably constant with latitude between ~1 and ~5 mbar. At lower altitudes, down into the tropopause region, we see that the south polar region is warmest; the mid-southern latitudes are cold, and the equator is relatively warm. The polar region, between ~65–70°, is enhanced by 7–8 K over the 10–100 mbar range, and by 5–6 K between 0.1 and 200 mbar. The equator is slightly ($\lesssim 1\,K$) warmer than the midlatitudes. Interestingly, Fletcher et al. (2014) show that the south polar region during the Voyager era was far less enhanced (by no more than 1–4 K) than observed by us in 2003 (see their Fig. 18).

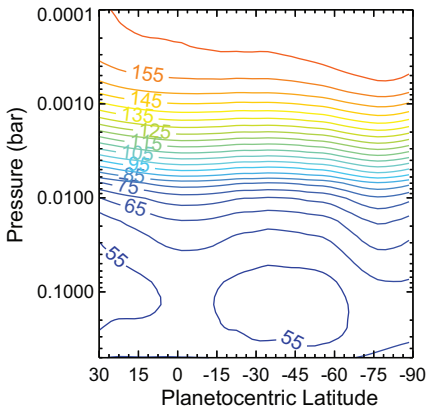

Fig. 15. Temperatures as retrieved from Keck/LWS imaging. The apparent cooling near the edges is caused by the beam dilution with deep space pixels. There is a clear cooling above southern midlatitudes, and heating above the south pole and the equator from the upper troposphere into the stratosphere (from Fletcher et al., 2014).

The latitudinal temperature variations induce winds that, in the geostrophic approximation, flow along isobars. Fletcher et al. (2014) use the nominal wind profile as measured from the Voyager data (Sromovsky et al., 2001a), and the thermal wind equation to calculate the vertical wind shear from Fig. 15. They show that, with the warm equator and warm south pole, both the broad retrograde jet at Neptune's equator and prograde jet around the pole should decrease in strength with altitude (see their Fig. 16 for details). The prograde jet around the pole is indicative of a polar vortex here.

The MIR results contribute information to our picture of the planet's global dynamics that pertain to its stratosphere and upper troposphere. The results reviewed here suggest upwelling with adiabatic cooling at midlatitudes and subsidence with compressional heating near the equator and south pole, similar to that suggested by Conrath et al. (1991) to explain the Voyager/IRIS data. We will expand on this in Section 6.

5. Data analysis: radio wavelengths

At radio wavelengths we detect thermal emission from tropospheric depths of a few up to $\gtrsim$50 bar. An increase in brightness indicates that deeper, warmer layers are probed, most likely caused by a decrease in the opacity of absorbers (e.g., NH_3, H_2S). In the following subsections we discuss our RT program and the results obtained for the disk-integrated spectrum and disk-resolved images.

5.1. Radiative-transfer modeling at radio wavelengths

The RT code used in this paper has been described and used most recently by de Pater et al. (2005b). We assume the atmosphere to be in thermochemical equilibrium. We calculate the atmospheric structure after specification of the temperature, pressure, and composition of one mole of gas at some deep level in the atmosphere – for Neptune we specify this at a depth of about 2000 bar, which is well below the condensation level of the deepest cloud layer. The model then steps up in altitude, in 1-km steps. At each level, the new temperature is calculated assuming a dry or appropriate wet adiabatic lapse rate, and the new pressure by using hydrostatic equilibrium. The partial pressures of the trace gases in the atmosphere are computed. In our RT code, the criterion for a trace gas to condense and for a cloud to form from the condensate is that the partial pressure of the trace gas exceeds its saturation vapor pressure, or equivalently, that the temperature be below the "dew point" of the trace gas. Note that this is not, in general, the criterion that is used in modeling cloud formation in the Earth's atmosphere, with a few exceptions. One exception is the formation of the clouds in a fog or marine layer. Generally, on Earth, clouds form at altitudes that are significantly higher than the altitude of the dew point so that the water droplets are

super-cooled and the partial pressure of the water vapor is much greater than the saturation vapor pressure. On Earth, air is often super-cooled by up to 20 K before clouds form. The super-cooling allows a water drop to overcome the energy barrier imposed by the large surface tension due to the drop's small radius of curvature. Moreover, cloud formation on Earth is greatly enhanced when the surface tension energy barrier is alleviated by the presence of nuclei for the vapor to condense on. Marine and fog layers form on Earth when there is a slow cooling (generally due to radiation) so that the water vapor/liquid transition is in a quasi-stationary quasi-equilibrium. Due in part to the quasi-equilibrium, water droplets that have already formed by condensation in the fog or marine layer can serve as nuclei for other droplets to form. Implicit in our RT code for Neptune is the assumption that the computed cloud layers form from quasi-equilibrium states, as the fog and marine layers on Earth do. In contrast, high-altitude clouds on Earth form when the vapor/liquid phases are out of equilibrium, often due to relatively large vertical velocities, so that condensation requires the super-cooling available at high altitudes. In Section 6, we argue that in addition to the low-lying, marine-like cloud layers that form at their dew points (and included in our RT codes), Neptune also has high-altitude clouds that form at much colder temperatures.

In Neptune's atmosphere we expect an aqueous ammonia solution cloud (H_2O–NH_3–H_2S) topped off with water ice, and clouds composed of ammonium hydrosulfide (NH_4SH) and hydrogen sulfide ice at higher altitudes, as shown in Fig. 16 for an atmosphere in which CH_4, H_2S and H_2O are enhanced by a factor of 30 above the protosolar C, S and O, respectively. Since the NH_4SH cloud forms as a result of a reaction between NH_3 and H_2S gases, the test for NH_4SH cloud formation is that the equilibrium constant of the reaction is exceeded. Both NH_3 and H_2S are reduced in equal molar quantities until the product of their atmospheric pressures equals the equilibrium constant. As the trace gases are removed from the atmosphere by condensation, "dry" air (an H_2–He mixture) is entrained into the parcel to ensure the mixing ratios add up to one. This cycle is repeated until the tropopause temperature is reached. We choose the temperature and pressure at our base level such that for every model the temperature is close to ~71.5 K at the 1 bar level (Voyager RSS; Lindal, 1992). The temperature profile together with abundance profiles for various gases are shown in Fig. 14; these were also used in the NIR and MIR RT calculations. In this figure we show two altitude profiles for methane gas: one for an abundance equal to 30× the solar C value, and one for 50× solar C. The latter profile was used in the NIR and MIR calculations; the temperature profile probed at NIR and MIR wavelengths is not noticeably different between an atmosphere where all CH_4, H_2S, and H_2O are enhanced by a factor of 50 or 30, or whether wet or dry (note that all profiles are 'anchored' at the 1 bar level at 71.5 K). Microwave spectra for both were shown in Fig. 7.

Cloud densities are computed like adiabatic liquid water contents for terrestrial clouds, i.e., they represent maximum cloud densities based on assuming no loss by precipitation. On Earth, precipitation may significantly lower the cloud density – up to factors of ~5 below the adiabatic cloud value (Pruppacher and Klett, 1980), and hence the actual cloud density at any location on Neptune is hard to predict. Globally averaged, however, the cloud density is likely several times or more below the adiabatic cloud value. Even if we would know the altitude and density of a cloud, not much is known about the microwave absorptivity of the clouds. Because of all these reasons we decided to ignore the direct effect of cloud opacity on the microwave spectrum, and include only the gas opacity. The potential effect of microwave absorption by clouds has been shown by e.g., de Pater et al. (1991) and de Pater and Mitchell (1993). The effect, when calculated for the maximum cloud densities, can be substantial, and the authors typically needed to decrease the cloud opacity by a factor of 3 to simulate giant planet microwave spectra. We further note that the microwave weighting functions all lie above the putative ammonia solution cloud; hence it is reasonable to ignore at least its cloud opacity.

The gas opacity in Neptune's atmosphere at mm–cm wavelengths is primarily determined by collision-induced absorption due to hydrogen gas (CIA: we include H_2–H_2, H_2–He, H_2–CH_4) and H_2S, while at wavelengths $\gtrsim$10 cm NH_3 and H_2O play some role (Fig. 7). Our code has been updated with the new laboratory measurements for microwave properties of NH_3 and H_2O vapor, which were obtained under simulated (high pressure) jovian conditions (Devaraj et al., 2011; Karpowicz and Steffes, 2011). For CIA we use the absorption coefficients calculated from revised ab initio models of Orton et al. (2007b), assuming an equilibrium distribution of the hydrogen para vs ortho states.

Although Neptune is only slightly oblate and differences in calculating the disk-averaged brightness temperatures for a spherical or ellipsoidal spheroid are small, the code now is using the ellipsoidal spheroid, and the line-of-sight pathlengths are corrected for refractive bending. This update was essential to calculate the emission from Neptune's south pole, as discussed further in Section 5.2. There is also an option to calculate the full gravity field including zonal winds; however, the difference with an ellipsoidal spheroid was negligible, so this option was not used. The pixel size in our full model is ~0.01″.

5.2. Radio results

Neptune's disk-averaged spectrum was shown in Fig. 7. Superposed are the models of Luszcz-Cook and de Pater (2013, see their Fig. 4), which used the RT code as described by de Pater et al. (2005b). In this paper these model spectra have been recomputed with the updates to the code as described in the previous section. A comparison of the curves labeled "CO" shows the effect of an

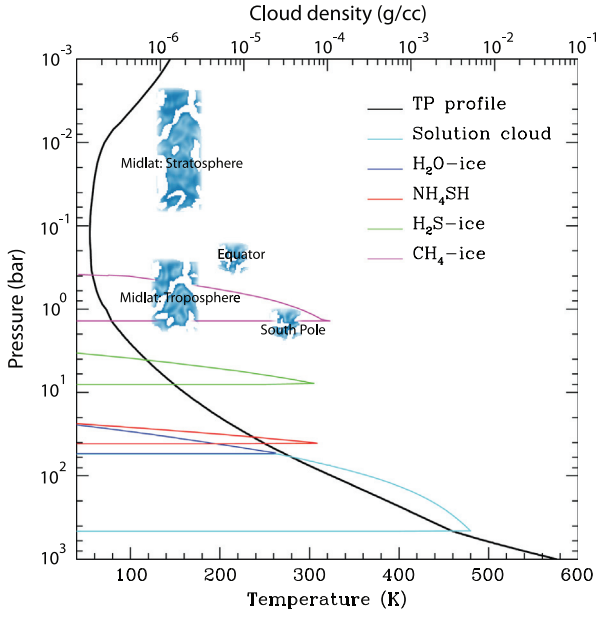

Fig. 16. Plot of the Temperature–pressure profile from Fig. 14 together with the cloud layers expected in Neptune's atmosphere, assuming thermochemical equilibrium and no loss of cloud particles due to precipitation. The approximate locations of the observed midlatitude, equatorial and south polar clouds are indicated.

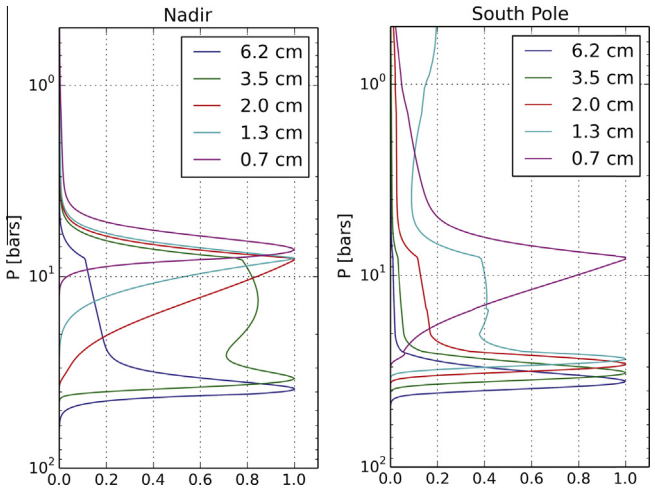

Fig. 17. Weighting functions at radio wavelengths for the nominal model (panel a; nadir viewing) and the hot spot (panel b; at its appropriate emission angle).

improvement in the general model; since opacity by CO is confined to only a few specific wavelengths at $\lambda \lesssim 3$ mm, the overall shape of these model curves is determined by CIA. Other curves on the plot show the effect of individual gases on the microwave spectrum. For example, the effect of H_2S dominates the spectrum from $\sim$1 mm up $\gtrsim$6 cm (note, though, that the NH_3 abundance is severely depleted compared to H_2S and H_2O; otherwise opacity by ammonia gas would dominate the spectrum). Absorption by H_2O is noticeable longwards of $\sim$1 cm if there are no other absorbers (except for H_2), and starts to effect the spectrum longwards of $\sim$10 cm in the presence of other absorbers; however, the effect by H_2O is negligible if there is even a tiny amount of NH_3 gas in the atmosphere. Overall, the differences between these model curves and those published by Luszcz-Cook and de Pater are very small. As shown, reasonable fits are obtained for an atmosphere dominated by a dry adiabatic lapse rate if the H_2S and H_2O are enhanced by a factor of 50 above the values for a protosolar composition atmosphere; if the atmosphere is characterized by a wet adiabat, good fits are obtained if the gas abundances are enhanced by a factor of 30.

In the following we used an atmosphere with a wet lapse rate, and enhancement factors for H_2S, H_2O and CH_4 of $\sim$30. Weighting functions for this nominal model atmosphere are shown in Fig. 17a, for nadir viewing. As shown, at radio wavelengths we probe depths from about 5 down to 50 bars at disk-center.

We used the new model for a horizontally (in longitude and latitude) homogeneous atmosphere to simulate our radio maps at all five wavelengths. Before comparison, we convolved the model maps with a circular gaussian-shaped beam, with a FWHM (full width at half maximum) as observed, and summarized in Table 5. Difference maps, i.e., observed minus model maps, are shown in Fig. 18. Such maps show the south polar hot spot most clearly. These maps further show a very good agreement in overall structure (e.g., brightness temperature and limb-darkening) between the models and the observations.

To determine the origin, depth and extent of the radio hot spot, we modeled it as a "plateau", or area of constant low opacity, centered at the south pole and extending outwards to different latitudes. A good fit to all data is obtained if the plateau extends over all latitudes and longitudes from 90°S up to 66°S. The modeled brightness temperature matches the observations very well if the H_2S abundance is depleted at these latitudes to 5% of its nominal

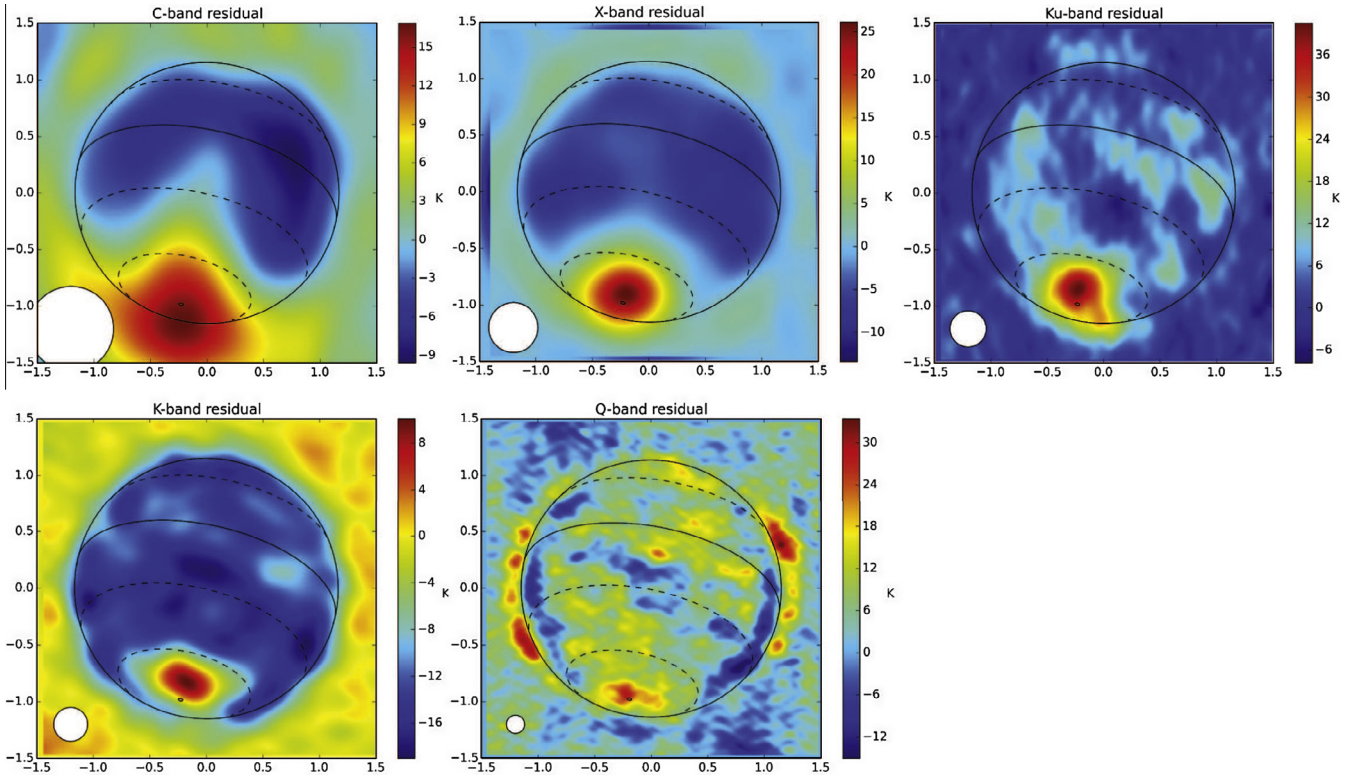

Fig. 18. Radio difference maps at the five wavelengths, where a uniform RT model was subtracted from the data. Note that, overall, such a uniform model matches both the absolute brightness temperature and the limb darkening at each wavelength very well. Latitude lines at 60°S, 30°S, the equator, and 30°N are indicated. Disk-averaged brightness temperatures were summarized in Table 6.

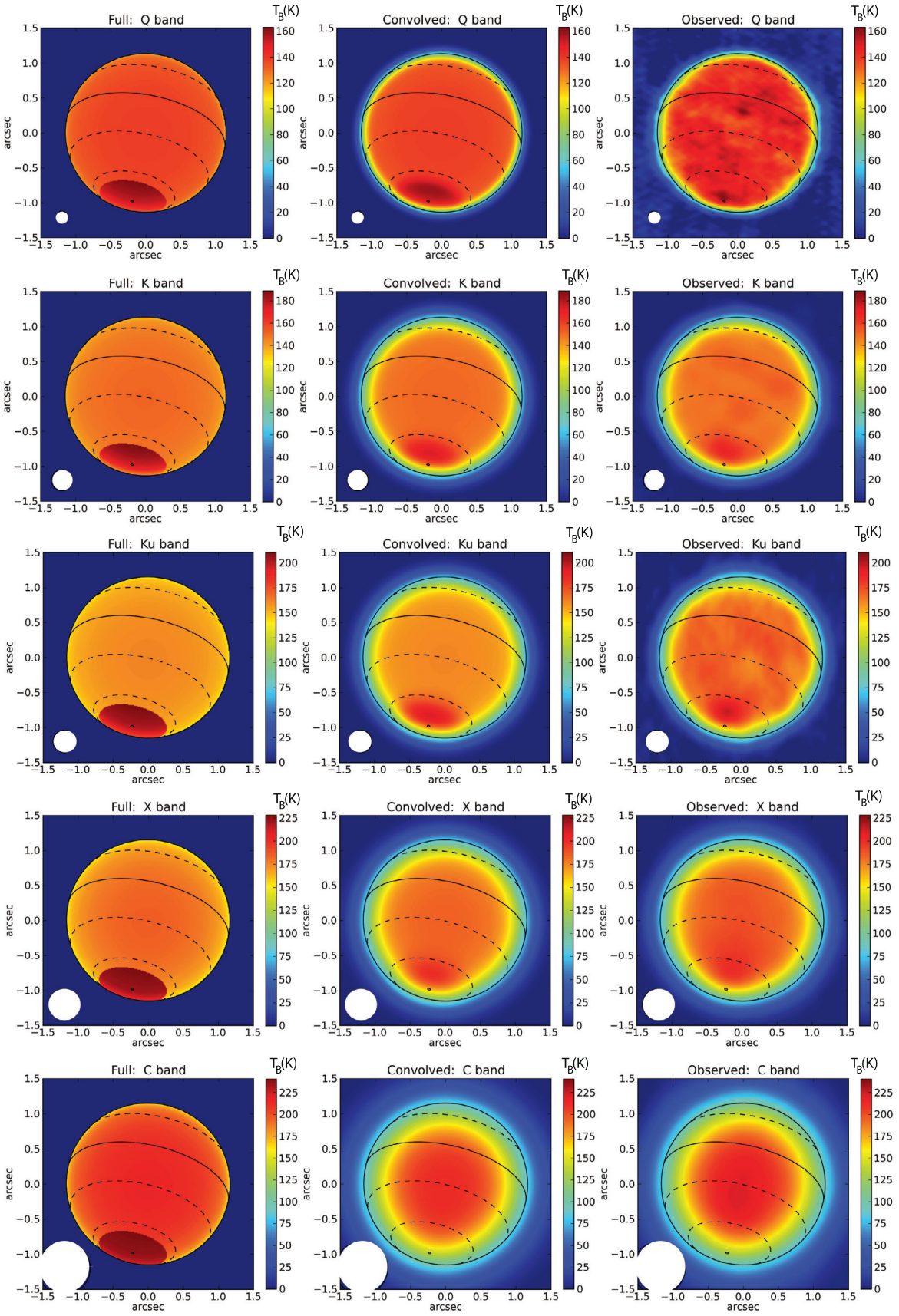

Fig. 19. Comparison of model maps with the data at radio wavelengths. Column 1 shows the model with enhanced brightness temperature at the polar region, from 90°S up to 66° S (best fit temperature, as shown in Fig. 21); this model, convolved with the appropriate beam (shown in the lower left corner) is shown in Column 2; Column 3 shows the observations. Latitude lines at 60°S, 30°S, the equator, and 30°N are indicated.

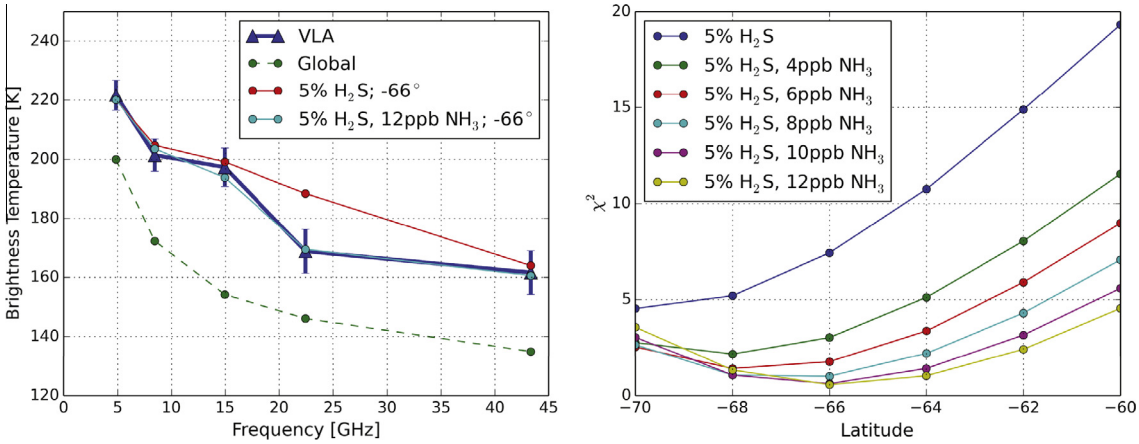

Fig. 20. Left panel: Comparison of the observations at the south pole (blue points/line), the nominal model at the south pole (green line), and two hot spot models at the south pole: the red line shows the resulting profile after decreasing the H_2S abundance to 5% of its nominal value above the NH_4SH cloud over all latitudes from 66°S to 90°S (Fig. 14); the cyan line shows results for the same H_2S profile, but adding 12 ppb NH_3 above the NH_4SH cloud. Right panel: χ^2 values for different south polar models as a function of the latitude lower boundary of the plateau over which the H_2S abundance is decreased. As shown, the plateau most likely extends out to a latitude of 66°S. (For interpretation of the references to color in this figure legend, the reader is referred to the web version of this article.)

value down to the level of the NH_4SH cloud, as shown by the green[5] dashed line in Fig. 14. The resulting models are shown in Column 1 of Fig. 19; these models convolved with the beam are shown in Column 2 and the observed maps are shown for comparison in Column 3.

We ran a number of different models to evaluate the uniqueness of our hot spot model. If the hot spot would be merely a point source at the south pole, we have to deplete H_2S gas down to at least 200 bar to match the observed temperature at 3.6 cm, after convolving the model with the beam. Such a model, however, does not fit all the data, nor does the location of the hot spot coincide with that observed; it appears to be at too low a latitude compared to the observations. Hence the hot region does appear to extend over a range of latitudes.

Fig. 20 shows a plot of the data at the south pole (blue), with superposed the nominal model at the proper emission angle (green) and the south polar Hot Spot model (red). When a small amount of NH_3 is aloft above the NH_4SH cloud layer (12 ppb), the observed profile can be matched exactly (cyan line in Fig. 20). In the right panel of Fig. 20 we evaluate various models with varying amounts of NH_3 aloft above the NH_4SH cloud, as a function of the lower boundary of the south polar plateau; i.e., we varied this boundary from $-70°$ to $-60°$, and calculated the χ^2 value for the various models. The best fit is obtained for a lower boundary of 66°S, and 12 ppb of NH_3 above the NH_4SH cloud.

Our derived value for H_2S above Neptune's south pole agrees well with the number derived by Luszcz-Cook et al. (2013) to simulate continuum maps of Neptune at 1.3 mm wavelength. The 1.3 mm continuum emission arises mostly from depths between 1 and 5 bars, i.e., slightly higher in the atmosphere than the data we present here. Luszcz-Cook et al. (2013) show that their data can also be matched if instead of a low H_2S abundance over the south pole, the methane abundance over the south pole is about four times lower than over southern midlatitudes (and eight times lower than at northern midlatitudes). Although methane itself does not absorb at mm wavelengths, it constitutes about 35% of the opacity due to CIA (for a 2.2% atmospheric methane abundance). The latter authors can also match their observations by assuming equilibrium conditions over the south pole, and subequilibrium conditions over southern midlatitudes. This scenario is consistent with that found from a reanalysis of the Voyager data by Fletcher et al. (2014). Based on the calculations by de Pater and Mitchell (1993) we expect that neither a latitudinal variation in the CH_4 abundance nor in the fraction of para-H_2 would be able to fully explain the microwave data, since the altitude range over which the opacity over the south pole is low has to extend down to the ~40 bar level, depths in Neptune's atmosphere where the ortho–para ratio in H_2 equals that of normal hydrogen.

The addition of a hot polar spot to the models will raise the disk-averaged brightness temperature by a few degrees K; these numbers are summarized in Table 6. As mentioned before, weighting functions in an atmosphere depend very much on the model atmosphere and the emission angle. In Fig. 17b we show the weighting functions for Neptune's south polar hot spot. The differences between the nominal model in panel (a) (nadir viewing) and the hot spot model (emission angle of the south pole) are quite pronounced. Due to the decrease in the H_2S abundance, all weighting functions are pushed down in the atmosphere (the change in emission angle alone would raise the weighting functions – as in Fig. 13).

6. Models of global circulation, clouds, and vortices derived from the multi-wavelength observations

In previous sections we presented and analyzed observations at NIR, MIR, and radio wavelengths. Each of the three Sections 3–5 was focused on the analysis of one particular wavelength regime, using RT codes specific to those wavelengths. In this section we use our observations from NIR, MIR and radio wavelengths *combined* to infer the three-dimensional global circulation of Neptune's atmosphere and to infer the physics responsible for the observed cloud patterns.

6.1. Physical assumptions

There are two sources of energy for Neptune's atmosphere: (1) solar heating, which varies in latitude and season, and (2) an unknown internal heating, which is approximately 170% of the solar heating. This energy is then re-distributed by other physics. Vertical plumes, due to convection, warm (cool) the air at locations where the plumes rise (sink) where the lapse rate is *super-adiabatic*. However, thermally forced global circulations, convective

[5] For interpretation of color in Fig. 14, the reader is referred to the web version of this article.

overshoots, local "weather", and local vortices also create vertically-aligned plumes in the *sub-adiabatic* atmosphere. In these regions, rising (sinking) plumes have the opposite effect of convectively driven plumes, and they locally cool (warm) the atmosphere. Other dynamics, including, gravity wave-breaking, phase changes (e.g., the formation and destruction of clouds), can heat and cool the atmosphere locally as well as move heat and chemical species up, down and sideways. The effect of the anomalous hot and cool spots and anomalous species concentrations that were created by these dynamics is to force the atmosphere to try to relax back to local thermal and chemical equilibrium. In anomalously warm (cool) regions, molecules emit more (less) than they absorb and cool (heat) the gas. Thus for example, we do not interpret excess brightness by some molecules as a *cause* of heating, but rather, as an *effect*.

One underlying assumption in the models proposed below is that the longitudinally-averaged thermal anomalies that have been observed in the troposphere and stratosphere are predominantly due to the adiabatic heating (cooling) from sinking (rising) vertical plumes in a sub-adiabatic atmosphere. This picture is in contrast to the view that the cause of the anomalously warm south pole is due to the Sun's summer-time heating (e.g., Orton et al., 2007a). Current observational uncertainties prohibit a quantitative comparison between these two scenarios at the south pole. However, we provide other evidence below that the atmospheric gases over the poles are subsiding, and this favors our adiabatic heating scenario.

A second underlying assumption, and a significant way in which our proposed model of Neptune's global circulation differs from previous models, is that Neptune's troposphere and stratosphere are strongly dynamically coupled. This coupling is illustrated in Fig. 21, which shows that the two global circulation cells in each hemisphere extend from ~40 bar in the troposphere, through the tropopause near 0.1 bar, to $\lesssim 10^{-4}$ bar in the stratosphere. Our hypothesis is that Neptune's atmosphere differs significantly from those of Saturn and Jupiter because the latter have tropopauses that differ qualitatively from Neptune's. In Saturn and Jupiter the temperature in the tropopause decreases near-adiabatically with decreasing pressure (increasing height) below the tropopause, but above the tropopause in the stratosphere, the temperature increases rapidly with decreasing pressure and increasing height (e.g., Fig. 4.1 in de Pater and Lissauer (2010)). The same trend is true in Neptune. However on Saturn and Jupiter, the tropopauses are sharply defined because dT/dP, the slope of P *vs* T, is nearly discontinuous at the tropopause where the slope abruptly changes sign. As Fig. 16 shows, this is not the case for Neptune. Neptune's tropopause is diffuse with the altitudes where dT/dP changes sign (i.e., where dT/dP is nearly zero and the atmosphere is nearly isothermal) extending over several pressure scale heights between ~0.01 bar and ~1.0 bar. Neptune's diffuse, rather than sharp, tropopause is dynamically significant. In numerical calculations in ideal gases (Marcus and Hassanzadeh, 2011) with sharp tropopauses similar to those in Saturn and Jupiter, vertically rising plumes (with velocities less than 5 m/s) from the troposphere never penetrate the tropopause. Rather, upon striking the tropopause, they diverge horizontally (like the mushroom clouds from the rising fireball of an atom bomb). In contrast, when the same numerical experiments were repeated with a diffuse tropopause, like that of Neptune, the vertical plumes pass through the tropopause and reach high altitudes in the stratosphere. In addition, the numerical experiments were not able to produce coherent vortices, or any type of long-lived circulation patterns, that straddled a sharp tropopause (with the bottom in the troposphere and the top in the stratosphere). However, coherent and long-lasting vortices

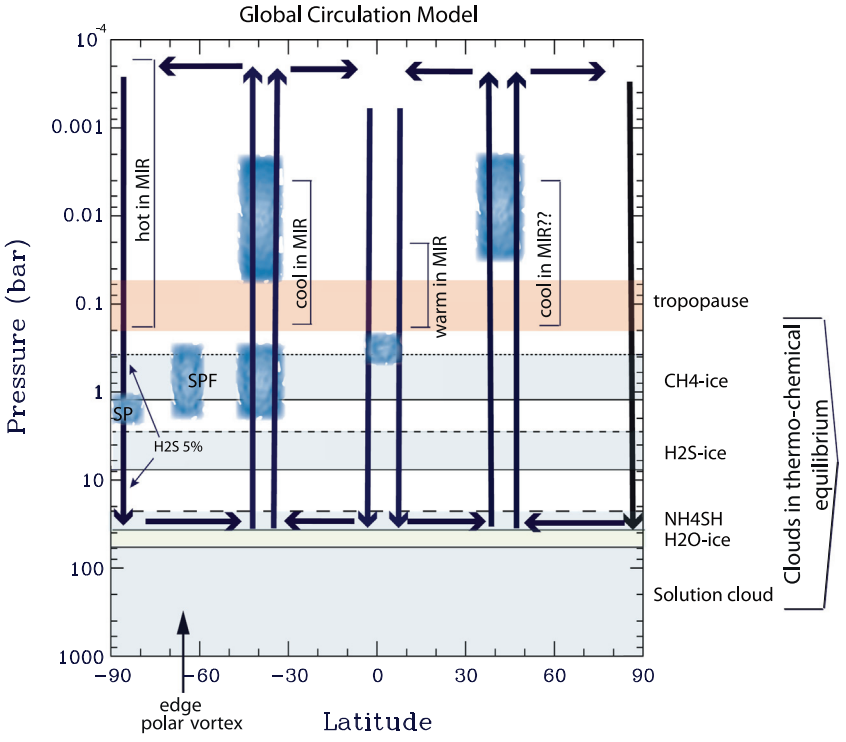

Fig. 21. Sketch of our proposed global circulation model. The various cloud layers (CH_4–ice, H_2S–ice, NH_4SH, H_2O–ice and the solution cloud) indicated on the graph are based on thermochemical equilibrium calculations, and are assumed to be independent of latitude. The tropopause is shown as a pink band, to convey that the tropopause is a rather broad isothermal region. The thick black arrows indicate the global circulation pattern, extending from $\lesssim$0.1 mbar down to over 40 bars. The clouds as observed at NIR wavelengths are indicated as vertical blue patches, roughly over the extent as indicated in Table 8 (using the minimum and maximum derived pressures). We indicated where, in the MIR, the observations showed high and low temperatures, and where, in the radio, we derived low humidities. We mirrored the circulation over the equator, assuming symmetry between the two hemispheres, as suggested by the observations at mid-northern latitudes. The edge of the south polar vortex is indicated by an arrow; the SPFs are located near this edge. (For interpretation of the references to color in this figure legend, the reader is referred to the web version of this article.)

and circulations could be produced that straddled a diffuse tropopause. These numerical experiments suggest that global circulations, like those in Fig. 21, that straddle the tropopause can exist on Neptune (but are not likely on Jupiter and Saturn).

6.2. Global circulation

As a consequence of mass conservation, vertical motions in the atmosphere, and the approximately axisymmetric nature of Neptune's atmosphere, Neptune's global circulation must have north–south motions as shown by the horizontal arrows in Fig. 21. Another consequence of mass conservation is that if the characteristic vertical velocities associated with rising and subsiding air are the same, then the areas of subsidence (i.e., the sum of the areas of two polar regions and the equatorial region) must be approximately equal to the areas with rising vertical velocities (i.e., the areas of the midlatitude regions in each hemisphere). This is consistent with the global circulation sketched in Fig. 21.

Variations in the longitudinally-averaged physical temperature across Neptune's disk can be discerned at MIR wavelengths. At radio wavelengths we measure latitudinal variations in the brightness temperature. Our analyses in the previous sections identified four anomalous warm and cool regions: (i) southern midlatitudes (∼20°–60°S), (ii) northern midlatitudes (∼20°–40°N), (iii) the equator (latitudes ∼ ±20°), and (iv) the south polar region (latitudes ∼66°–90°S).

- *Southern midlatitudes*. While MIR observations reveal a relatively uniform temperature structure (along isobars) in the lower stratosphere between ∼1 and 5 mbar, at lower altitudes, down to ∼200 mbar, the temperature is ∼5 K lower above southern midlatitudes than over other regions, indicative of adiabatic cooling, i.e., rising motions at these altitudes.
- *Northern midlatitudes*. Although it is more difficult to derive the temperature structure from MIR data at the northern latitudes, an anomalous cool region, implying rising air, is consistent with observations.
- *Equator*. MIR observations reveal that the temperature above the equator is anomalously warm by a few degrees K in the lower stratosphere (∼20–100 mbar) and upper troposphere, indicating subsiding air.
- *South polar region*. Thermal emission at MIR wavelengths indicates that the south pole is the warmest spot on the planet. The south polar region from ∼66°S down to the pole is enhanced in temperature by 5–6 K between 0.1 and 200 mbar. At radio wavelengths the brightness temperature of this region is enhanced by ∼20–40 K. The radio images can be best reproduced with radiative transfer (RT) models when the anomalous warm region covers the entire area from the south pole down to a latitude of 66°S. This warm plateau can be matched with RT models at radio wavelengths when the H_2S abundance is 5% of its saturated vapor pressure value above the NH_4SH cloud, i.e., the atmosphere's relative humidity in H_2S is 5% above the south polar region. At radio wavelengths this low humidity allows one to probe deeper, warmer layers in Neptune's atmosphere. This low humidity is suggestive of subsiding air. Condensible gases in the vertically rising branches of the circulation at the midlatitudes (Fig. 21) will condense at altitudes where the temperatures correspond to their dew points. Above these altitudes, the humidities may be at 100% (i.e., saturated air). After the north–south components of the global circulation in the stratosphere carry the gas to the equator and poles, the descending gas at low altitudes will be dry and have low relative humidities. Hence the observations at both MIR and radio wavelengths imply subsiding air over the south polar region, from the stratosphere (∼0.1 mbar) down into the deep troposphere ($\gtrsim$40 bar).

The vertical motions implied by these observations at different wavelengths and locations, the north–south velocities implied by mass conservation, and symmetry with respect to the equator are the basis of the 2-cell per hemisphere circulation shown in Fig. 21. This circulation is similar to the findings by Conrath et al. (1991) and Bézard et al. (1991) based on Voyager IRIS data. However, there is one important difference. Our proposed general circulation extends over a much larger range in altitude, from (tens of) microbars in the stratosphere down to tens of bars in the troposphere. Previous models were confined to the stratosphere and upper troposphere (down to perhaps the ∼1 bar level).

Other observations corroborate the global circulation in Fig. 21. The spatial distribution of the ortho/para-H_2 ratio derived by Fletcher et al. (2014) from the Voyager/IRIS data show anomalous sub-equilibrium concentrations of para-H_2 at both the southern and northern midlatitudes and super-equilibrium concentrations of para-H_2 above the equator and south pole. These anomalous concentrations indicate upwelling and subsidence that are in accord with Fig. 21. Our radio maps do not show an equatorial brightening, and therefore do not indicate low humidity supporting the existence of a sinking motion over the equator as shown in our proposed general circulation in Fig. 21. However, a new map at ∼1 cm recently obtained with the upgraded VLA does show such an equatorial brightening (Butler et al., 2012), and therefore supports the picture of equatorial subsidence extending from the stratosphere down into the deep troposphere (∼5–10 bar).

Our suggestion of a circulation model that extends over many scale heights may help explain some of Karkoscka's (2011a,b) findings. In his 2011b paper, he analyzed HST-WFPC2 images at different wavelengths taken between 1994 and 2008, and noticed large changes in activity on time scales of ∼5 years, which seemed to be correlated over 4 scale heights. In his 2011a paper he analyzed Neptune's South Polar Features and South Polar Waves (SPFs and SPWs) in Voyager and >20 years of HST data, and found that a large structure of latitudinal motions has been stationary with the System II rotational period for over 20 years. He suggests that this may be explained by a deep convective pattern.

Our simple global circulation model cannot explain all data, however. The above mentioned 1 cm map of Neptune also shows a slight enhancement in the radio brightness temperature at mid-southern latitudes, indicative of relatively dry air. In addition, from an analysis of HST–STIS data Karkoschka and Tomasko (2011) found that the methane abundance at these mid-southern latitudes is low between 1.2 and 3.3 bar compared to the deep atmosphere and the equator. This suggests that the circulation is more complicated than the simple one suggested above, since it appears as if there must be some subsiding air at these latitudes.

6.3. Vortices and clouds

Here we show that the observations of clouds and vortices, as well as our inferences of where vortices are located in the atmosphere, are consistent with our proposed general circulation in Fig. 21. Our cloud observations and interpretations can be summarized:

6.3.1. Southern midlatitude, high and low-altitude clouds

NIR images show striking banded patterns of clouds. The cloud tops were measured to reside at *two* different altitudes: in the stratosphere at ∼20–30 mbar, and at lower altitudes in the troposphere, at pressures $P \gtrsim 300$ mbar, with one bright cloud as deep

as 1.6 bar. Note that these two cloud layers are near the bottom and top of the almost isothermal region in the atmosphere, straddling the tropopause.

In accord with the global circulation in Fig. 21, these latitudes have an upwelling atmosphere. We first consider an explanation of the lower cloud deck. Rising air cools, and when the temperature drops below the condensation temperature of a particular gas, it is possible that a cloud of that composition will form. As stated in Section 5.1, on Earth clouds form at many distinct altitudes, and generally those altitudes do not correspond to altitudes where a gas's partial pressure equals its saturation vapor pressure, i.e., at its dew point. Here we propose that the cloud tops at midlatitudes at $P \gtrsim 300$ mbar are fog-like clouds that form at the low altitudes where the slowly upwelling flow of the global circulation first reaches the altitudes where the trace gas is at its dew point. In this scenario the clouds that we detected at NIR wavelengths are the tops of the marine-like fog layers, or patches of fog, where the layers are piled up on one another in an inhomogeneous way, so that the opacity/fog-thickness varies spatially. Because we cannot measure the composition of these clouds directly, we can at best infer their composition from thermochemical equilibrium calculations. The NIR-derived altitudes, and our assumption that the cloud deck is at the altitude where the gas is at its dew point, suggests a methane composition of these clouds (Figs. 16 and 21).

We argue that the high altitude clouds in the lower stratosphere at altitudes between ~20 and 30 mbar are *not* fog-like. These clouds form at altitudes that are well above the altitude where the gas's partial pressure equals its saturation vapor pressure. We propose that the high-altitude clouds are the analogs of the scattered clouds on Jupiter that are associated with its long-lived anticyclones. Laboratory studies (Marcus, 1990), as well as jovian observations (Marcus, 1993), show that anticyclones thrive at latitudes where the zonal flow is also anticyclonic. Neptune has a broad anticyclonic zonal flow between 10–60°S (Limaye and Sromovsky, 1991; Sromovsky et al., 1993; Hammel and Lockwood, 1997), so it is reasonable to assume that anticyclones are present at these latitudes. On Jupiter, robust anticyclones are observed in the upper troposphere, whereas we propose that on Neptune, they are at 20–30 mbar, i.e., in the lower stratosphere. Marcus (1993) showed that anticyclones on Jupiter form in anticyclonic zonal shears where a plume, rising through the atmosphere, decelerates as it enters the more stratified upper atmosphere. The deceleration causes the plume's vertical velocity v_z to decrease, making $\partial v_z/\partial z < 0$. The deceleration activates the Coriolis term, $f(\partial v_z/\partial z)$, in the equation that governs the rate at which vertical vorticity is created (Pedlosky, 1982), where f is the Coriolis parameter. (This is the same Coriolis term that creates whirlpools in a bathroom sink where $\partial v_z/\partial z$ becomes large as the water goes down the drain.) This Coriolis force can copiously create anticyclonic vorticity at the midlatitudes (where f is large) at altitudes where the plume decelerates. On Jupiter, a plume rising through the troposphere cannot penetrate the tropopause, and rapidly decelerates there, causing vortices to form just beneath the tropopause (where they are observed), but not in the stratosphere (where they are not observed). On Neptune, we expect the deceleration of rising plumes at the southern midlatitudes to also produce anticyclones. However, Neptune's tropopause is too diffuse to totally arrest rising plumes, so much of their deceleration must occur in the stratosphere. In particular, we propose that there are decelerations near ~20–30 mbar, the altitudes of the southern midlatitude's high clouds. We discussed (Marcus, 2004; de Pater et al., 2010) that anticyclones in the presence of thermal radiation create secondary flows with vertical velocity components. These local vertical motions are in addition to the global circulation. At the center in the top half of the anticyclones air is rising past the top of the anticyclone itself (Marcus et al., 2013a,b; see Fig. 8 in Wong et al., 2011). This local upwelling adiabatically cools the atmosphere and that cooling can lead to cloud formation at the top of the anticyclone. A similar picture of cloud formation above anticyclones was first posed by Flasar et al. (1981). On Neptune, we suggest that the midlatitude stratospheric clouds are the tops of anticyclones. In our picture, the altitudes of the high-altitude clouds are not determined by the altitude of the atmosphere's dew point, but rather, by the altitudes of the tops of the anticyclones. The condensibles in the gas in the anticyclone's upwelling plume that forms the clouds are not in thermal quasi-equilibrium, but are super-cooled well below their dew points.

The above scenarios for the low-lying fog-like clouds and the sporadic stratospheric clouds would explain our observations of clouds at the southern midlatitudes that show the seemingly paradoxical appearance of high-altitude clouds adjacent to low-altitude clouds. Our scenario argues that we are looking at scattered high-altitude clouds over a background of low-altitude patches of fog. Below this fog layer is an optically thick cloud (at ~2.4 bar). As mentioned above, this cloud model agrees well with the haze layers suggested by Luszcz-Cook (2012). Gibbard et al. (2003) proposed that the stratospheric clouds could have formed through condensation of hydrocarbons near the tropopause. Irwin et al. (2011) suggested that methane, rising up from below, could condense on hydrocarbon haze particles in the stratosphere and thus form the stratospheric clouds.

We do not believe that the high-altitude clouds at midlatitudes are associated with local convective storms because convective storms are usually associated with cyclonic disturbances. Cyclones are not only unstable, but in general, cannot be in equilibrium when they are located in strong anticyclonic zonal shear flows, such as those at Neptune's midlatitudes (Marcus, 1990). Note that on Jupiter (Little et al., 1999, Fig. 7) and Saturn (Fischer et al., 2011), observations of lighting that have been attributed to local convective storms are always in regions of strong cyclonic shear rather than anticyclonic zones.

6.3.2. Northern midlatitudes

NIR images also reveal prominent bands of clouds at northern midlatitudes. These clouds are in the stratosphere, near the ~10 mbar level, i.e., at slightly higher altitudes than those seen at southern midlatitudes. As shown in Fig. 15, this may be caused by the low temperatures extending over a somewhat larger altitude range in the north than over southern midlatitudes; the tropopause itself does not appear to be shifted in altitude. Assuming that Neptune has an approximate hemispheric symmetry, we suggest that these high-altitude clouds are similar to those in the southern hemisphere.

6.3.3. Equator

At NIR wavelengths the equatorial region is largely devoid of clouds, although a few relatively faint clouds have been detected there. These clouds are typically located in the upper troposphere, near pressures of 250–350 mbar. The relative dearth of clouds near the equator might be due to the overall sinking motion of the global circulation which adiabatically heats and dries the atmosphere. In addition, the lack of clouds near the equator could be due to the lack of cyclonic storms. The Coriolis parameter f goes to zero at the equator, so cyclonic vorticity cannot be easily created by the Coriolis term $f(\partial v_z/\partial z)$. The weak or non-existent f is the accepted explanation for why hurricanes on Earth do not form close to its equator (Emanuel, 1994), and similarly explained why the Great Dark Spot on Neptune (Lebeau and Dowling, 1998) and the large storm system (the 'Berg') on Uranus (de Pater et al., 2011) disappeared after moving in the direction of the equator.

6.3.4. South pole

At or near the south pole is a small cloud feature that has its cloud top close to the 2 bar level. Luszcz-Cook et al. (2010) noted that Neptune's south polar cloud sometimes is visible as two clouds, and may be offset from the pole. They compare Neptune's south pole to Saturn's south pole, the latter of which is characterized by a region of subsidence at the eye (e.g., Fletcher et al., 2008), surrounded by two concentric eyewalls near 88°S which extend up to the tropopause (Dyudina et al., 2009). The latter authors show that inside and outside of this wall are discrete bright clouds that are confined to the lower troposphere; they compare these to the heavily precipitating clouds encircling the eye of terrestrial hurricanes. As suggested by Luszcz-Cook et al., the cloud at Neptune's south pole may be analogous to the eye of Saturn's south polar vortex. Just like on Saturn, this cloud is in the lower troposphere, and is the deepest cloud seen on Neptune. Given its pressure level, it may originate in the H_2S cloud (Fig. 16).

6.3.5. South polar region (66–90°S)

If the polar subsidence shown in Fig. 21 accelerates as it descends from the stratified stratosphere into the weakly-stratified troposphere, then $\partial v_z/\partial z > 0$, and the cyclonic vorticity generated by the Coriolis term $f(\partial v_z/\partial z)$ will reinforce a cyclonic vortex at the south pole. The velocities extracted from Voyager (Limaye and Sromovsky, 1991) and HST (Hammel and Lockwood, 1997) tie-points obtained from tropospheric clouds show that a strong polar vortex extends from the pole to ~60–70°S, where there is a maximum in the prograde (eastward traveling) winds. Fletcher et al. (2014) observed a sharp radial temperature gradient in the polar stratosphere near these latitudes. We suggest that this boundary is at the same latitude as the edge of the radio-dry polar region at 66°. These findings coupled with the thermal wind equation (Pedlosky, 1982) indicates that there is a strong vertical shear in the east–west winds at this latitude. While it may be by chance that this latitude is also the same as the outer boundary of the tropospheric south polar vortex, we think it is not a coincidence, and that the stratospheric observations suggest that the south polar tropospheric vortex is not inhibited by Neptune's diffuse tropopause, but rather extends across the tropopause into the stratosphere.

6.3.6. South Polar Features at 60–70°

Several cloud features, known as South Polar Features or SPFs, are seen along or just outside the periphery of the polar vortex. The facts that these clouds are located in the troposphere and are centered at 60–70°S strongly suggest that they are bright cumulus clouds associated with convective cyclonic storms. In regions of weak, stable stratification, we expect Neptune, like Jupiter and Saturn, to have intermittent regions of local convection driven from below by an internal heat source. Neptune emits a thermal flux about 2.6 times larger than the mean solar flux absorbed by its atmosphere (Pearl and Conrath, 1991). We argue that the most likely region for local convective storms on Neptune is 60–70°S because those latitudes have many of the ingredients that produce convective storms on Earth. The strongest horizontal wind shears and vertical vorticities are at 60–70°S near the peak prograde jet that surrounds the polar vortex. If the cyclonic east–west winds south of the peak become intermittently unstable, then the cyclonic vertical vorticity of the winds can "roll-up" into cyclonic storms. In particular, instabilities in an atmosphere can broadly be categorized into two types: *baroclinic* (a local, vertical turning over of the fluid that can occur when the fluid density is not constant on isobaric surfaces) and *barotropic* (instabilities generally associated with horizontal wind shears, not local buoyancy, and driven by the kinetic energy of the winds). The latitudes at 60–70°S are susceptible to both types. Barotropic instabilities would be expected because there is a local maximum and a local minimum of the potential vorticity of the east–west winds on the southern and northern sides, respectively, of the peak prograde jet near 66°S. The Rayleigh-Kuo theorem (Drazin and Reid, 2004) states that a necessary condition to produce linear barotropic instability is that the potential vorticity of the winds has a local maximum or minimum. Moreover, the barotropic instability is centered at the latitudes of the extrema. Baroclinic instabilities would be expected because there is a strong baroclinic front near ~66°S where the cooler, denser air of the midlatitudes abuts the warmer, more buoyant air of the south polar vortex. As mentioned above, Fletcher et al. observed directly the front as a sharp radial temperature gradient in the stratosphere near 66°S. Due to the presence of all of these ingredients, we suggest that the latitudes near 66°S are likely to create local convective storms. Like Neptune's high-altitude, midlatitude clouds, we would not expect the altitudes of the storm clouds at 60–70°S to be at their dew point. Rather, their altitudes are determined by the altitudes of their associated convective storms. SPFs are highly variable in brightness, with time scales on the order of hours (e.g., Sromovsky et al., 1993; Rages et al., 2002). These time scales are consistent with the lifetimes of terrestrial, convectively-driven cumulus clouds (Cotton and Anthes, 1991).

7. Summary

Between June and October 2003 we observed Neptune at near- and mid-infrared wavelengths with both 10-m W.M. Keck telescopes, and at radio wavelengths with the Very Large Array. Our goal was to constrain Neptune's global dynamics from $\lesssim 0.1$ mbar levels down to tens of bars. At mid-infrared and radio wavelengths Neptune's thermal emission is observed over this range of altitudes; in the near-infrared we receive sunlight reflected off clouds and hazes in the upper troposphere and lower stratosphere.

Our findings can be summarized as follows:

- Neptune's stratosphere is characterized by a relatively uniform temperature structure (along isobars) at ~1–5 mbar. At lower altitudes there is a clear (by ~5 K) cooling above southern midlatitudes (~20–60°S). The south polar region (66°–90°S) is enhanced in temperature by 5–6 K between 0.1 and 200 mbar. At radio wavelengths this region is enhanced in brightness temperature by 20–40 K. In the lower stratosphere (~20–100 mbar) and upper troposphere the temperature is enhanced by a few degrees K above the equator.
- At NIR wavelengths we find three different layers of cloud-top features above an optically thick ($\tau = 10$) cloud at 2.4 bar: Deep ($P > 1$ bar) features, perhaps rising up from the H_2S ice cloud; features at pressures $P \sim 0.2$—0.6 bar; and features in the stratosphere, at $P \sim 10$—30 mbar. There is an overall trend that the deepest features are located in the south, and the highest (~10 mbar) in the north. At southern midlatitudes we find both, sometimes adjacent, tropospheric and stratospheric clouds. Although one might expect such clouds to induce a dispersion in the winds measured at these latitudes, our MIR observations (Fletcher et al., 2014), like the Voyager data, suggest a near-zero vertical wind shear at these latitudes. We propose the low-level southern midlatitude clouds to be the tops of fog-like or marine-like layers composed of methane-ice at the altitude of the dew point, and the high altitude stratospheric clouds to be the tops of anticyclones.
- In agreement with previous authors (e.g., Conrath et al., 1991; Bézard et al., 1991), we suggest a global circulation pattern of air rising at both northern and southern midlatitudes, and

descending over the south pole and the equator. In contrast to previous authors, however, we suggest this circulation to extend from the stratosphere ($\lesssim$0.1 mbar levels) down to tens of bars in the troposphere. This model is sketched in Fig. 21. Adiabatic cooling is prevalent at latitudes where air is rising, both in the troposphere and the stratosphere; this cooling is seen in the MIR, and cloud condensation is prominent in the NIR. Adiabatic heating is seen over regions where air is descending; the south pole and the equator are warm, as sensed at MIR wavelengths, and these regions are generally relatively free of clouds. Since the descending air is much dryer than rising air, deeper warmer layers in the atmosphere are probed at radio wavelengths, resulting in enhanced brightness temperatures over the pole. The radio data suggest that the subsiding air is dry, at only 5% relative humidity of H_2S above the NH_4SH cloud, which is at ~40 bar. The warm polar vortex extends from the south pole down to latitudes of 66°S.

- We suggest that the region near the southern hemisphere's prograde jet has baroclinic instabilities that promote cyclonic convective storms and that the bright transient features near 60–70°S, the South Polar Features (SPFs), are the clouds associated with those storms.

Acknowledgments

We thank L. Sromovsky and two anonymous referees for valuable comments to help improve our manuscript. Some of the data presented were obtained at the W.M. Keck Observatory, which is operated as a scientific partnership among the California Institute of Technology, the University of California and the National Aeronautics and Space Administration. The Observatory was made possible by the generous financial support of the W.M. Keck Foundation. This work has been supported in part by the National Science Foundation Science and Technology Center for Adaptive Optics, managed by the University of California at Santa Cruz under cooperative Agreement No. AST 9876783, and by NSF Grant AST-0908575 to UC Berkeley. S.H.L.C. is supported by the Kalbfleisch Postdoctoral Fellowship at the American Museum of Natural History. L.N.F. is supported by a Royal Society Research Fellowship at the University of Oxford. P.S.M. is supported in part by AST-1009907 and by NASA PATM grants NNX10AB93G and NNX13AG56G. The authors wish to recognize and acknowledge the very significant cultural role and reverence that the summit of Mauna Kea has always had within the indigenous Hawaiian community. We are most fortunate to conduct observations from this mountain.

Appendix A. A planet's brightness temperature

Since the planet blocks the cosmic background (CMB) radiation, the brightness temperature as measured at radio wavelengths is lower than the true brightness temperature. Even when observing a planet with an interferometer, i.e., resolving out large scale structures such as the CMB, the planet's brightness temperature is measured with respect to the background, and hence the brightness temperature of the CMB should be added to that measured of the planet. The planet's flux density as measured on the sky, F_ν, therefore consists of the difference of the flux density of that planet with a brightness temperature, T_b, and the flux density of the CMB with a brightness temperature T_{CMB} (we adopt $T_{CMB} = 2.725$ K):

$$F_\nu = \frac{2h\nu}{c^3}\left(\frac{1}{e^{h\nu/kT_b}-1} - \frac{1}{e^{h\nu/kT_{CMB}}-1}\right)\frac{\pi R_{eq}R_{p'}}{\Delta^2}, \tag{4}$$

where h is Planck's constant, c the speed of light, k Boltzmann's constant, Δ is the distance to the planet, and R_{eq} and $R_{p'}$ are the equatorial and apparent polar radii of the planet. The apparent polar radius depends on the true polar radius, R_p, and the sub-Earth latitude, ϕ:

$$R_{p'} = \sqrt{\left(R_{eq}^2 \sin^2\phi + R_p^2\cos^2\phi\right)}. \tag{5}$$

We can solve this equation in steps to find the brightness temperature:

$$\frac{1}{e^{h\nu/kT_b}-1} = \frac{1}{e^{h\nu/kT_{CMB}}-1} + \frac{F_{nu}c^2\Delta^2}{2h\nu^3\pi R_{eq}R_{p'}}, \tag{6}$$

which, after re-arranging, results in:

$$T_b = \frac{h\nu}{k}\left[ln\left(1 + \frac{1}{\frac{1}{e^{h\nu/kT_{CMB}}-1} + \frac{F_\nu c^2\Delta^2}{2h\nu^3\pi R_{eq}R_{p'}}}\right)\right]^{-1}. \tag{7}$$

We used $R_{eq} = 24,766$ km and $R_p = 24,342$ km for Neptune's equatorial and polar radii, resp. (Lindal, 1992), which for a sub-Earth latitude of $-29°$ results in $R_{p'} = 24,442$ km. The resulting brightness temperatures are summarized in Table 6.

Although the above method is by far the most accurate way to correct a planet's brightness temperature for the CMB, we used a "shortcut" for older data that had not been corrected for the CMB (see e.g., Gibson et al., 2005). We determined the flux density for the CMB at frequency ν, $F_{\nu_{CMB}}$:

$$F_{\nu_{CMB}} = \frac{2h\nu}{c^3}\frac{1}{e^{h\nu/kT_{CMB}}-1}. \tag{8}$$

We then converted this flux density into a Rayleigh–Jeans equivalent brightness temperature:

$$T_{CMB} = \frac{c^2}{2k\nu^2}F_{\nu_{CMB}}. \tag{9}$$

This temperature, T_{CMB}, varying from 0.1 K at a wavelength of 1.1 mm up to 2.07 K at 1.0 cm and 2.69 K at 20 cm, was added to the brightness temperature that was originally reported.

References

Ádámkovics, M., de Pater, I., Hartung, M., Eisenhauer, F., Genzel, R., Griffith, C.A., 2006. Titan's bright spots: Multiband spectroscopic measurement of surface diversity and hazes. J. Geophys. Res. 111, E07S06.

Ádámkovics, M., de Pater, I., Hartung, M., Barnes, J.W., 2009. Evidence for condensed-phase methane enhancement over Xanadu on Titan. Planet. Space Sci. 57, 1586–1595.

Asay-Davis, X.S., Marcus, P.S., Wong, M.H., de Pater, I., 2009. Jupiter's evolving Great Red Spot: Velocity measurements with the advection corrected correlation image velocimetry automated cloud tracking method. Icarus 203, 164–188.

Asplund, M., Grevesse, N., Sauval, A.J., Scott, P., 2009. The chemical composition of the Sun. Ann. Rev. Astron. Astrophys. 47, 481–522.

Baines, K.H., Mickelson, M.E., Larson, L.E., Ferguson, D.W., 1995. The abundances of methane and ortho/para hydrogen in Uranus and Neptune: implications of new laboratory 4-0 H_2 quadrupole line parameters. Icarus 114, 328–340.

Bézard, B., Romani, P.N., Conrath, B.J., Maguire, W.C., 1991. Hydrocarbons in Neptune's stratosphere from Voyager infrared observations. J. Geophys. Res. 96 (18), 961–1897.

Borysow, A., 1991. Modeling of collision-induced infrared absorption spectra of H_2–H_2 pairs in the fundamental band at temperatures from 20 to 300 K. Icarus 92, 273–279.

Borysow, A., 1992. New model of collision-induced infrared absorption spectra of H–He pairs in the 2–2.5 micron range at temperatures from 20 to 300 K – An update. Icarus 96, 169–175.

Borysow, A., 1993. Erratum: "Modeling of collision-induced infrared absorption spectra of H_2–H_2 pairs in the fundamental band at temperatures from 20 to 300 K/″" [Icarus 92(2), 273–279 (August 1991)]. Icarus 106, 6–14.

Borysow, J., Trafton, L., Frommhold, L., Birnbaum, G., 1985. Modeling of pressure induced far-infrared absorption spectra molecular hydrogen pairs. Astrophys. J. 296, 644–654.

Borysow, J., Frommhold, L., Birnbaum, G., 1988. Collision-induced rototranslational absorption spectra of H_2–He pairs at temperatures from 40 to 3000 K. Astrophys. J. 326, 509–515.

Butler, B.J., Steffes, P.G., Suleiman, S.H., Kolodner, M.A., Jenkins, J.M., 2001. Accurate and consistent microwave observations of Venus and their implications. Icarus 154, 226–238.

Butler, B.J., Hofstadter, M., Gurwell, M., Orton, G., Norwood, J., 2012. The deep atmosphere of Neptune from EVLA observations. Bull. Am. Astron. Soc. 44. Abstract #504.06.
Clark, B.G., 1980. An efficient implementation of the algorithm 'CLEAN'. Astron. Astrophys. 89, 377–378.
Cohen, M., Walker, R.G., Carter, B., Hammerseley, P., Kidger, M., Noguchi, K., 1999. Spectral irradiance calibration in the infrared. X. A self-consistent radiometric all-sky network of absolutely calibrated stellar spectra. Astrophys. J. 117, 1864–1889.
Colina, L., Bohlin, R.C., Castelli, F., 1996. The 0.12–2.5 micron absolute flux distribution of the Sun for comparison with solar analog star. Astron. J. 112, 307–315.
Conrath, B.J. et al., 1989. Infrared observations of the neptunian system. Science 246, 1454–1459.
Conrath, B.J., Flasar, F.M., Gierasch, P.J., 1991. Thermal structure and dynamics of Neptune's atmosphere from Voyager measurements. J. Geophys. Res. 96, 18931–18939.
Conrath, B.J., Gautier, D., Owen, T.C., Samuelson, R.E., 1993. Constraints on N_2 in Neptune's atmosphere from Voyager measurement. Icarus 101, 168–171.
Cotton, W.R., Anthes, R.A., 1991. Storm and Cloud Dynamics. Academic Press.
deBoer, D.R., Steffes, P.H.G., 1996. Estimates of the tropospheric vertical structure of Neptune based upon microwave radiative transfer studies. Icarus 123, 324–335.
de Pater, I., Lissauer, J.J., 2010. Planetary Sciences, second ed. Cambridge University Press, pp. 647.
de Pater, I., Mitchell, D.L., 1993. Microwave observations of the planets: The importance of laboratory measurements. Geophys. Res. Planets 98, 5471–5490.
de Pater, I., Richmond, M., 1989. Neptune's microwave spectrum from 1 mm to 20 cm. Icarus 80, 1–13.
de Pater, I., Romani, P.N., Atreya, S.K., 1991. Possible microwave absorption by H_2S gas in Uranus and Neptune's atmospheres. Icarus 91, 220–233.
de Pater, I., Gibbard, S.G., Chiang, E., Hammel, H.B., Macintosh, B., Marchis, F., Martin, S.C., Roe, H.G., Showalter, M., 2005a. The dynamic neptunian ring arcs: Evidence for a gradual disappearance of Liberté and resonant jump of courage. Icarus 174, 262–272.
de Pater, I., DeBoer, D.R., Marley, M., Freedman, R., Young, R., 2005b. Retrieval of water in Jupiter's deep atmosphere using microwave spectra of its brightness temperature. Icarus 173, 425–438.
de Pater, I., Gibbard, S.G., Hammel, H.B., 2006. Evolution of the dusty rings of Uranus. Icarus 180, 186–200.
de Pater, I., Wong, M., Marcus, P.S., Luszcz-Cook, S., Adamkovics, M., Conrad, A., Asay-Davis, X., Go, C., 2010. Persistent rings in and around Jupiter's anticyclones – Observations and Theory. Icarus 210, 742–762. http://dx.doi.org/10.1016/j.icarus.2010.07.027.
de Pater, I., Sromovsky, L.A., Hammel, H.B., Fry, P.M., LeBeau, R.P., Rages, K., Showalter, M., Matthews, K., 2011. Post-equinox observations of Uranus: Berg's evolution, vertical structure, and track towards the equator. Icarus 215, 332–345.
Devaraj, K., Steffes, P.G., Karpowicz, B.M., 2011. Reconciling the centimeter- and millimeter-wavelength ammonia absorption spectra under jovian conditions: Extensive millimeter-wavelength measurements and a consistent model. Icarus 212, 224–235.
Drazin, P.G., Reid, W.H., 2004. Hydrodynamic Stability. Cambridge University Press.
Dyudina, U.A. et al., 2009. Saturn's south polar vortex compared to other large vortices in the Solar System. Icarus 202, 240–248.
Elias, J.H., Frogel, J.A., Matthews, K., Neugebauer, G., 1982. Infrared standard stars. Astron. J. 87, 1029–1034.
Emanuel, K.A., 1994. Atmospheric Convection. Oxford University Press.
Fischer, G., 2011. Overview of Saturn lightning observations. In: Planetary, Solar and Heliospheric Radio Emissions (PRE VII), pp. 135–144.
Fitzpatrick, P.J., de Pater, I., Luszcz-Cook, S.H., Wong, M.H., Hammel, H.B., 2013. Dispersion in Neptune's zonal wind velocities from Astrophys, NIR Keck AO observations in July 2009. Space Sci. 350, 65–88.
Flasar, F.M., Conrath, B.J., Pirraglia, J.A., Clark, P.C., French, R.G., Gierasch, P.J., 1981. Thermal structure and dynamics of the jovian atmosphere 1. The Great Red Spot. J. Geophys. Res. 86, 8759–8767.
Fletcher, L.N. et al., 2008. Temperature and composition of Saturn's polar hot spots and hexagon. Science 319, 79–81.
Fletcher, L.N., de Pater, I., Orton, G.S., Hammel, H.B., Sitko, M.L., Irwin, P.G.J., 2014. Neptune at summer solstice: Zonal temperatures from ground-based observations, 2003–2007. Icarus 231, 146–167.
Fry, P.M., Sromovsky, L.A., 2004. Keck 2 AO observations of Neptune in 2003 and 2004. Bull. Am. Astron. Soc. 36, 1103.
Gibbard, S.G., de Pater, I., Roe, H.G., Macintosh, B., Gavel, D., Max, C.E., Baines, K.H., Ghez, A., 2002. High-resolution infrared imaging of Neptune from the Keck telescope. Icarus 156, 1–15.
Gibbard, S.G., de Pater, I., Roe, H.G., Martin, S., Macintosh, B.A., Max, C.E., 2003. The altitude of Neptune cloud features from high-spatial-resolution near-infrared spectra. Icarus 166, 359–374.
Gibson, J., Welch, Wm.J., de Pater, I., 2005. Accurate jovian flux measurements at λ1 cm show ammonia to be sub-saturated in the upper atmosphere. Icarus 173, 439–446.
Gulkis, S.M., Janssen, M.J., Olsen, E.T., 1978. Evidence for the depletion of ammonia in the Uranus atmosphere. Icarus 34, 10–19.
Hackwell, J.A., Warren, D.W., Chatelain, M.A., Dotan, Y., Li, P.H., 1990. A low resolution array spectrograph for the 2.9 to 13.5 micron spectral region. Proc. SPIE 1235, 171–180.
Hammel, H.B., 1989. Discrete cloud structure on Neptune. Icarus 80, 14–22.
Hammel, H.B., Lockwood, G.W., 1997. Atmospheric structure of Neptune in 1994, 1995 and 1996: HST imaging at multiple wavelengths. Icarus 80, 416–438.
Hammel, H.B., Lockwood, G.W., Mills, J.R., Barnet, C.D., 1995. Hubble Space Telescope imaging of Neptune's cloud structure in 1994. Science 268, 1740–1742.
Hammel, H.B., Lynch, D.K., Russell, R.W., Sitko, M.L., Bernstein, L.S., Hewagama, T., 2006. Mid-infrared ethane emission on Neptune and Uranus. Astrophys. J. 644, 1326–1333.
Hammel, H.B. et al., 2007. Distribution of ethane and methane emission on Neptune. Astron. J. 134, 637–641.
Hofstadter, M.D., 1992. Microwave imaging of Neptune. Bull. Amer. Astron. Soc. 24, 973.
Irwin, P. et al., 2008. The NEMESIS planetary atmosphere radiative transfer and retrieval tool. J. Quant. Spectrosc. Radiat. Transfer 109 (6), 1136–1150.
Irwin, P.G.J., Teanby, N.A., Davis, G.R., Fletcher, L.N., Orton, G.S., Tice, D., Hurley, J., Calcutt, S.B., 2011. Multispectral imaging observations of Neptune's cloud structure with Gemini-North. Icarus 216, 141–158.
Jones, B., Puetter, R.C., 1993. Keck long-wavelength spectrometer. In: Fowler, A.M. (Ed.), Infrared Detectors and Instrumentation. Proc. SPIE, vol. 1946, pp. 610–621.
Karkoscka, E., 2011a. Neptune's rotational period suggested by the extraordinary stability of two features. Icarus 215, 439–448.
Karkoscka, E., 2011b. Neptune's cloud and haze variations 1994–2008 from 500 HST-WFPC2 images. Icarus 215, 759–773.
Karkoschka, E., Tomasko, M.G., 2011. The haze and methane distributions on Neptune from HST–STIS spectroscopy. Icarus 211, 780–797.
Karpowicz, B.M., Steffes, P.G., 2011. In search of water vapor on Jupiter: Laboratory measurements of the microwave properties of water vapor under simulated jovian conditions. Icarus 212, 210–223.
Kellermann, K.I., Pauliny-Toth, I.I.K., 1966. Observations of the radio emission of Uranus, Neptune and other planets at 1.9 cm. Astrophys.J. 145, 954–957.
Kloosterman, J.L., Butler, B., de Pater, I., 2008. VLA observations of Jupiter's synchrotron radiation at 15 GHz. Icarus 193, 644–648.
Lebeau, R.P., Dowling, T.E., 1998. EPIC simulations of time-dependent, threedimensional vortices with application to Neptune's Great Dark Spot. Icarus 132, 239–265.
Lellouch, E. et al., 2010. First results of Herschel-PACS observations of Neptune. Astron. Astrophys. 518, L152–L155.
Lewis, J.S., Prinn, R.G., 1980. Kinetic inhibition of CO and N_2 reduction in the solar nebula. Astrophys. J. 238, 357–364.
Lii, P.S., Wong, M.H., de Pater, I., 2010. Temporal variation of the tropospheric cloud and haze in the jovian equatorial zone. Icarus 209, 591–601.
Limaye, S.S., Sromovsky, L.A., 1991. Winds of Neptune – Voyager observations of cloud motions. J. Geophys. Res. Suppl. 96, 18941–18960.
Lindal, G.F., 1992. The atmosphere of Neptune: An analysis of radio occultation data acquired with Voyager 2. Astron. J. 103, 967–982.
Little, B., Anger, C.D., Ingersoll, A.P., Vasavada, A.R., Senske, D.A., Breneman, H.H., Borucki, W.J., the Galileo SSI Team, 1999. Galileo images of lightning on Jupiter. Icarus 142, 306–323.
Luszcz-Cook, S.H., 2012. Millimeter and Near-Infrared Observations of Neptune's Atmospheric Dynamics. Ph.D. Thesis, UC Berkeley, December 2012.
Luszcz-Cook, S.H., de Pater, I., 2013. Constraining the origins of Neptune's carbon monoxide abundance with CARMA millimeter-wave observations. Icarus 222, 379–400.
Luszcz-Cook, S.H., de Pater, I., Adamkovics, M., Hammel, H.B., 2010. Seeing double at Neptune's south pole. Icarus 208, 938–944.
Luszcz-Cook, S.H., de Pater, I., Wright, M., 2013. Spatially-resolved millimeter-wavelength maps of Neptune. Icarus 226, 437–454.
Marcus, P.S., 1990. Vortex dynamics in a shearing zonal flow. J. Fluid Mech. 215, 393–430.
Marcus, P.S., 1993. Jupiter's Great Red Spot and other vortices. Annu. Rev. Astron. Astrophys. 31, 523–573.
Marcus, P.S., 2004. Prediction of a global climate change on Jupiter. Nature 428, 828–831.
Marcus, P., Hassanzadeh, P., 2011. 3D vortices in stratified, rotating flows-secondary circulations and changes in aspect radio due to dissipation. Bull. Am. Phys. Soc. 64. Abstract #A1.003.
Marcus, P.S., Pei, S., Jiang, C.-H., Hassanzadeh, P., 2013a. Self-replicating three-dimensional vortices in neutrally-stable stratified rotating shear flows. Phys. Rev. Lett. 111, 084501. http://dx.doi.org/10.1103/PhysRevLett.111.084501.
Marcus, P.S., Asay-Davis, X., Wong, M.H.D., de Pater, I., 2013b. Jupiter's Red Oval BA: Dynamics, color, and relationship to jovian climate change. J. Heat Transfer 135, 1–9. http://dx.doi.org/10.1115/1.4007666.
Martin, S., de Pater, I., Kloosterman, J., Hammel, H.B., 2008. Multi-wavelength observations of Neptune's atmosphere. EPSC2008-A-00277.
Martin, S.C., de Pater, I., Marcus, P., 2012. Neptune's zonal winds from near-IR Keck adaptive optics imaging in August 2001. Astrophys. Space Sci. 337, 65–78.
Max, C.E. et al., 2003. Cloud structures on Neptune observed with Keck telescope adaptive optics. Astron. J. 125, 364–375.
Mitchell, J.L., Ádámkovics, M., Caballero, R., Turtle, E.P., 2011. Locally enhanced precipitation organized by planetary-scale waves on Titan. Nat. Geosci. 4, 589–592.
Orton, G.S., Encrenaz, T., Leyrat, C., Puetter, R., Friedson, A.J., 2007a. Evidence for methane escape and strong seasonal and dynamical perturbations of Neptune's atmospheric temperatures. Astron. Astrophys. 473, L5–L8.

Orton, G.S., Gustafsson, M., Burgdorf, M., Meadows, V., 2007b. Revised ab initio models for H_2–H_2 collision-induced absorption at low temperatures. Icarus 189, 544–549.
Orton, G.S. et al., 2012. Recovery and characterization of Neptune's near-polar stratospheric hot spot. Planet. Space Sci. 61, 161–167.
Pedlosky, J., 1982. Geophysical Fluid Dynamics. Springer-Verlag, New York and Berlin, 636 pp..
Pearl, J.C., Conrath, B.J., 1991. The Albedo, effective temperature and energy balance of Neptune, as determined from Voyager data. J. Geophys. Res. 96, 18921–18930.
Rages, K., Hammel, H.B., Lockwood, G.W., 2002. A prominent apparition of Neptune's South Polar Feature. Icarus 159, 262–265.
Pruppacher, H.R., Klett, J.D., 1980. Microphysics of Clouds and Precipitation. D. Reidel Publishing Company, Dordrecht Holland, 714 pp..
Roddier, F., Roddier, C., Graves, J.E., Northcott, M.J., Owen, T., 1998. NOTE: Neptune's cloud structure and activity: Ground-based monitoring with adaptive optics. Icarus 136, 168–172.
Roe, H.G., 2002. Titans Atmosphere at High Resolution. Ph.D. Thesis, University of California, Berkeley.
Roe, H.G. et al., 2001. The altitude of an infrared bright cloud feature on Neptune from near-infrared spectroscopy. Astron. J. 122, 1023–1029.
Smith, B.A. et al., 1989. Voyager 2 at Neptune: Imaging science results. Science 246, 1422–1449.
Sromovsky, L.A., Limaye, S.S., Fry, P.M., 1993. Dynamics of Neptune's major cloud features. Icarus 105, 110–141.
Sromovsky, L.A., Limaye, S.S., Fry, P.M., 1995. Clouds and circulation on Neptune: Implications of 1991 HST observations. Icarus 118, 25–38.
Sromovsky, L.A., Frye, P.M., Dowling, T.E., Baines, K.H., Limaye, S.S., 2001a. Coordinated 1996 HST and IRTF imaging of Neptune and Triton. III. Neptune's atmospheric circulation and cloud structure. Icarus 149, 459–488.
Sromovsky, L.A., Fry, P.M., Dowling, T.E., Baines, K.H., Limaye, S.S., 2001b. Neptune's atmospheric circulation and cloud morphology: Changes revealed by 1998 HST imaging. Icarus 150, 244–260.
Sromovsky, L.A., Fry, P.M., Limaye, S.S., Baines, K.H., 2003. The nature of Neptune's increasing brightness: Evidence for a seasonal response. Icarus 163, 256–261.
Sromovsky, L.A., Fry, P.M., Boudon, V., Campargue, A., Nikitin, A., 2012. Comparison of line-by-line and band models of near-IR methane absorption applied to outer planet atmospheres. Icarus 218, 1–23.
Wizinowich, P.L. et al., 2000. First light adaptive optics images from the Keck II telescope: A new era of high angular resolution imagery. Publ. Astron. Soc. Pacific 112 (769), 315–319.
Wong, M.H., de Pater, I., Marcus, P.S., Asay-Davis, X., Go, C.Y., 2011. Vertical structure of Jupiter's Oval BA before and 1 after it reddened: What changed? Icarus 215, 211–225.